European Variscan orogenic evolution as an analogue of Tibetan-Himalayan orogen: Insights from petrology and numerical modeling

P. Maierová, K. Schulmann, O. Lexa, S. Guillot, P. Štípská, V. Janoušek, O. Čadek

AGU PUBLICATIONS

Tectonics

RESEARCH ARTICLE
10.1002/2015TC004098

Key Points:
- P-T and geochemical data from Tibet-Himalaya and European Variscides show striking similarities
- Similarities are in (ultra)potassic magmatism and in two-stage metamorphic evolution of lower crust
- Modeling shows that evolution of the lower crust can be explained by gravity-driven exchanges

Supporting Information:
- Supporting Information S1

Correspondence to:
P. Maierová,
petra.maierova@geology.cz

Citation:
Maierová, P., K. Schulmann, O. Lexa, S. Guillot, P. Štípská, V. Janoušek, and O. Čadek (2016), European Variscan orogenic evolution as an analogue of Tibetan-Himalayan orogen: Insights from petrology and numerical modeling, *Tectonics*, *35*, 1760–1780, doi:10.1002/2015TC004098.

Received 7 DEC 2015
Accepted 28 JUN 2016
Accepted article online 4 JUL 2016
Published online 29 JULY 2016

European Variscan orogenic evolution as an analogue of Tibetan-Himalayan orogen: Insights from petrology and numerical modeling

P. Maierová[1,2], K. Schulmann[1,2], O. Lexa[3], S. Guillot[4], P. Štípská[1,2], V. Janoušek[2], and O. Čadek[5]

[1]EOST, Institute de Physique de Globe, UMR 7516, Université de Strasbourg, Strasbourg, France, [2]Center for Lithospheric Research, Czech Geological Survey, Prague 1, Czech Republic, [3]IPSG, Faculty of Science, Charles University, Prague 2, Czech Republic, [4]ISTerre, CNRS, Université Grenoble Alpes, Grenoble Cedex 09, France, [5]Faculty of Mathematics and Physics, Department of Geophysics, Charles University in Prague, Prague 8, Czech Republic

Abstract The European Variscan orogeny can be compared to the Tibetan-Himalayan system for three main reasons: (1) The Variscan belt originated through progressive amalgamation of Gondwanan blocks that were subsequently squeezed between the Laurussia and Gondwana continents. Similarly, the Tibetan-Himalayan orogen results from amalgamated Gondwanan blocks squeezed between Asia and India. (2) The duration of the collisional period and the scale of the two orogens are comparable. (3) In both cases the collisional process resulted in formation of a thick crustal root and long lasting high-pressure granulite facies metamorphism. Recent petrological data allow a more detailed comparison pointing to similarities also in the midcrustal re-equilibration of the granulites and their association with specific (ultra)potassic magmatic rocks. In both orogens, the origin of the granulites was attributed to relamination and thermal maturation of lower crustal allochthon below upper plate crust. Subsequent evolution was explained by midcrustal flow eventually leading to extrusion of the high-grade rocks. We propose that the lower and middle crustal processes in hot orogens are connected by gravity overturns. Such laterally forced gravity-driven exchanges of material in the orogenic root were already documented in the Variscides, but the recent data from Tibet and Himalaya show that this process may have occurred also elsewhere. Using numerical models, we demonstrate that the exchange of the lower and middle crust can be efficient even for a minor density inversion and various characteristics of the crustal layers. The modeled pressure-temperature paths are compatible with two-stage metamorphism documented in Tibet and Himalaya.

1. Introduction

Traditionally, the European Variscan belt has been considered as an ancient analogue of modern collisional orogens such as the Tibetan-Himalayan system [*Dewey and Burke*, 1973; *Matte et al*., 1990]. The main reason for which the Variscan and Tibetan-Himalayan systems can be correlated is that both orogens originated from amalgamation of Gondwanan continental fragments to the northern Laurussia or Eurasian continents during Paleozoic and Mesozoic-Tertiary times, respectively [*Collins*, 2003]. Separation of Gondwanan ribbons, their northward drift and successive amalgamation with northern continental mass are typical of the Pangean realm interior orogens [*Murphy and Nance*, 2008] hallmarking collisional tectonics (Figure 1). They show the following similarities: the double-thickened crust [e.g., *Jiménez-Munt et al*., 2008; *Schulmann et al*., 2014], bivergent orogenic geometry [e.g., *Yin and Harrison*, 2000], ultrahigh-pressure (UHP) metamorphism [e.g., *O'Brien et al*., 2001; *Kotková et al*., 2011; *Faryad and Žák*, 2016], orogenic root of granulite composition [*O'Brien and Rötzler*, 2003; *Guy et al*., 2011], and upper crustal low-grade units interpreted in the European Variscan belt as relics of a Tibetan-style orogenic plateau [*Dörr and Zulauf*, 2010].

The comparison of the two systems has not gone into more detail, partly because of fundamentally different ways we observe them. In the modern Tibet-Himalaya (TH), the internal structure is hidden beneath an upper crustal lid coinciding with the Tibetan Plateau. It is only at the topographic slopes along the southern flank of the orogen—a place of intense erosion—where rocks coming from the interior of the orogen crop out [e.g., *Hodges*, 2000]. Besides the restricted geological observations, the state and structure of the orogenic interior have been studied using geophysical methods, which can constrain the existence of principal crustal layers, density distribution, thermal state, and degree of melting of thickened crust [e.g., *Nelson et al*., 1996; *Hetényi et al*., 2007, 2011; *Hacker et al*., 2014]. Important sources of information are direct observations of the size and

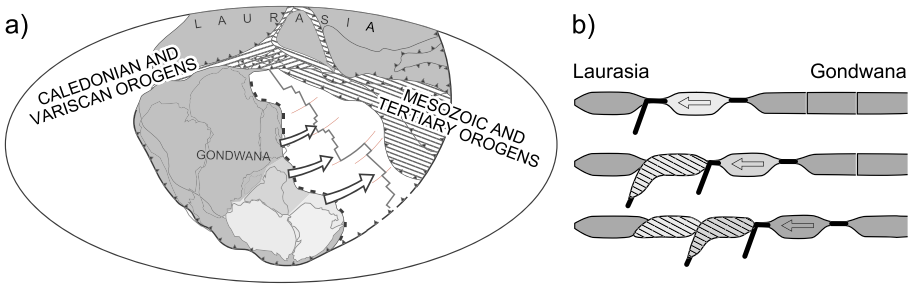

Figure 1. (a) Simplified map of the Pangea supercontinent [*Collins*, 2003; *Stampfli et al*., 2013] at Triassic times showing Gondwanan blocks amalgamated to Laurussia during the Paleozoic (SW-trending hatching) and progressive Mesozoic to Tertiary amalgamation to Laurasia (NW-trending hatching). (b) A sketch showing progression of amalgamation-collision process valid for both the Paleozoic and Mesozoic-Tertiary orogenies.

shape of the orogen, its topography, boundaries of tectonic units, and geodetically constrained surface motions [*Zhang et al*., 2004], which give guidance for understanding the global-scale tectonic evolution [*Tapponnier et al*., 2001].

In contrast, the internal architecture of a fossil orogen, such as the European Variscides, can be observed directly in a deeply eroded section and can be characterized by geophysical methods as well [e.g., *Schulmann et al*., 2014]. Geological methods can then constrain the pressure-temperature (*P-T*) evolution and deformation history of individual tectonic units, but putting these pieces of information into a large-scale picture resembles solving a puzzle. Geophysical methods are less decisive in this case, because they reveal the present state, which is, in contrast to the modern orogens, only a remnant of the formerly active zone. However, if all available data are put together, many details hidden in the modern orogens can be recognized.

Numerical experiments play a complementary role to observations in providing insight into dynamics of the orogenic systems. Numerical models addressing the TH evolution mostly rely on geophysical observations and on general knowledge of plate tectonics. They reproduce formation of a bivergent orogen, growth of a topographic plateau and its collapse [e.g., *England and McKenzie*, 1982; *Beaumont et al*., 2001], and address principal mechanisms shaping the orogen: midcrustal channel flow, continental subduction, or delamination of the mantle lithosphere [e.g., *Beaumont et al*., 2001; *Toussaint et al*., 2004; *Gray and Pysklywec*, 2012]. The geological data are also incorporated in some of the models, which focus mainly on the Barrovian-type metamorphism, timescales, and kinematics of metamorphic rocks exhumed in the Himalaya [*Jamieson et al*., 2004] or exhumation of UHP rocks during early stages of the collision [*Beaumont et al*., 2009].

Numerical models of ancient orogenies are still relatively rare and in the case of the European Variscides include only a handful of studies [e.g., *Willner et al*., 2002; *Maierová et al*., 2014; *Dymkova et al*., 2016]. Other considerations about their dynamics are inferred from generic-type models such as subduction wedge or gravity inversions [*Gerya et al*., 2000; *Gerya and Stöckhert*, 2006] or models designed for modern orogens [e.g., *Beaumont et al*., 2001]. Here we present a complementary approach: based on similarities between the TH orogen and the European Variscides, we suggest that a mechanism well constrained and modeled in the case of the Variscides [*Maierová et al*., 2014] might operate also in the TH.

2. Geological and Geophysical Constraints

In order to compare the two orogens we provide a summary of principal geological and geophysical constraints and main features of their geodynamic evolutions.

2.1. Tibetan-Himalayan System

2.1.1. Geology and Geophysics

The Tibetan Plateau (Figure 2a) is a 1000–1300 km wide area of elevated topography coinciding with a major gravity low of ~500 mGal. The crustal thickness reaches ~80 km in South Tibet and decreases toward the Qiangtang block, where the high topography is also supported by thinning of the mantle lithosphere [e.g., *Jiménez-Munt et al*., 2008]. In the southcentral Tibetan Plateau (Lhasa and Qiangtang blocks), seismic studies

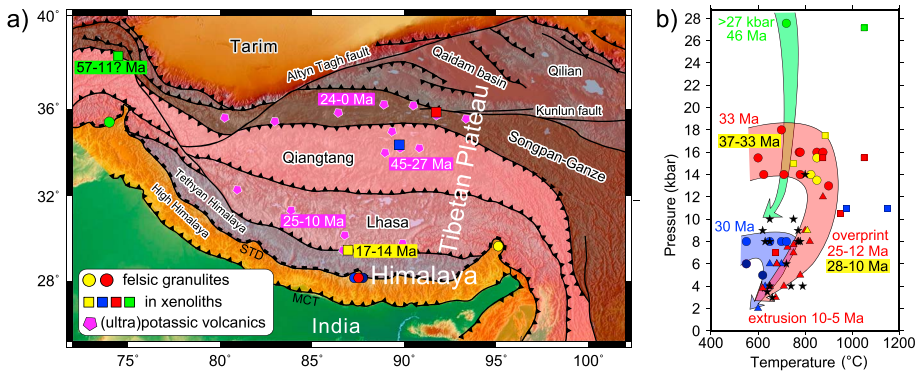

Figure 2. Tibetan-Himalayan system: geotectonic map and *P-T*(-time) conditions. (a) Geotectonic map of the Tibetan Plateau, the Himalaya, and adjacent continental blocks with positions of terranes, main sutures, and thrust zones [*Tapponnier et al*., 2001]. Distribution of (ultra)potassic volcanics (purple pentagons), crustal xenoliths (squares), and high-pressure rocks in South Tibet and Himalaya (circles). Age ranges show dating of (ultra)potassic volcanism in individual terranes (purple) and dating of granulites in xenoliths (green and yellow). (b) Peak conditions in xenoliths and in granulites retrieved from xenoliths in the Tibetan Plateau (squares). Red path shows evolution of eclogites and granulites in south Tibetan migmatitic domes from peak conditions (red and yellow circles) toward their re-equilibration (triangles) with surrounding migmatites. Green path shows early UHP metamorphic stage. Blue path corresponding to data from midcrustal gneisses (blue circles) overlaps with conditions in migmatites (asterisks). Colors of symbols correspond to those in Figure 2a. Xenolith data from *Jolivet et al*. [2003] (red), *Hacker et al*. [2000] (blue), *Chan et al*. [2010] (yellow), and *Hacker et al*. [2005] (green); HP rocks data from *Guilmette et al*. [2011] (yellow), *Kali et al*. [2010] and references therein (red), and *Guillot et al*. [2008] (green); volcanics data from *Chung et al*. [2005], *Ding et al*. [2007], and *Liu et al*. [2014].

show a significant decrease of *S* wave velocities in the depth range of 20–40 km [*Kind et al*., 1996], forming a low-velocity zone [*Nelson et al*., 1996], and occurrence of strong reflectors, called bright spots, at a depth of 20–25 km [e.g., *Brown et al*., 1996; *Alsdorf et al*., 1998]. In addition, magnetotelluric surveys show a drop of resistivity within the low-velocity zone [*Wei et al*., 2001]. All these data have been interpreted in terms of partial melting at ~20–40 km depth and melt accumulation in the apical part of the partially molten region [e.g., *Nelson et al*., 1996; *Schilling and Partzsch*, 2001]. *Hacker et al*. [2014] calculated that 2 % of silicate melt provide a good match to the low *S* wave velocities and anisotropy observed at 25–45 km depth beneath Qiangtang. However, *Hetényi et al*. [2011] pointed out the discontinuous character of the molten region with a maximum horizontal extent of individual patches of about 50 km and questioned the hypothesis of widespread partial melting.

The heat flow at the Plateau is elevated to ~90 mW m^{-2}, which is a common value in tectonically active regions, and locally exceeds ~150 mW m^{-2} [*Artemieva*, 2006] suggesting recent high-temperature conditions in the deep crust. The high thermal conditions of the lower crust and mantle prevailed over most of the Cenozoic as shown by studies of lower crustal xenoliths collected from (ultra)potassic volcanics dated at 40–0.5 Ma (squares in Figure 2b). These xenoliths are dominated by mafic to felsic granulites equilibrated at ~800–1100°C and ~8–17 kbar with rare eclogites [*Hacker et al*., 2000; *Jolivet et al*., 2003; *Ding et al*., 2007; *Chan et al*., 2010] (Figure 2b, squares). There are indications that the pressure variations are related to re-equilibration of granulites at pressures of 6–8 kbar prior to sampling by volcanic eruptions [*Jolivet et al*., 2003]. The high temperatures were interpreted to result from reheating of the base of the crust by (ultra) potassic magma, which is a mixture of metasomatized upper mantle-derived and lower crustal anatectic melts [*Turner et al*., 1996; *Chung et al*., 2005; *Ding et al*., 2007].

Earliest metamorphism related to India and Asia convergence was recorded along the northern margin of the subducting Indian plate at around 55–45 Ma. It reached UHP conditions of ~27 kbar at 700–770°C [*Guillot et al*., 2008, and references therein]. Late Eocene (37–33 Ma) high-temperature and high-pressure (HP) conditions (~20–14 kbar at ~800°C; red and yellow circles in Figure 2b) were also reported from eclogites and granulites of south Tibetan Neogene migmatitic domes [*Kali et al*., 2010, and references therein; *Guilmette et al*., 2011]. These rocks re-equilibrated at high-temperature midpressure conditions with surrounding migmatites from 28 to 10 Ma (triangles and asterisks in Figure 2b), coevally with the development of an amphibolite facies metamorphism along the Main Central Thrust [e.g., *Pognante et al*., 1993; *Groppo et al*., 2007; *Kali et al*., 2010; *Zhang et al*., 2010].

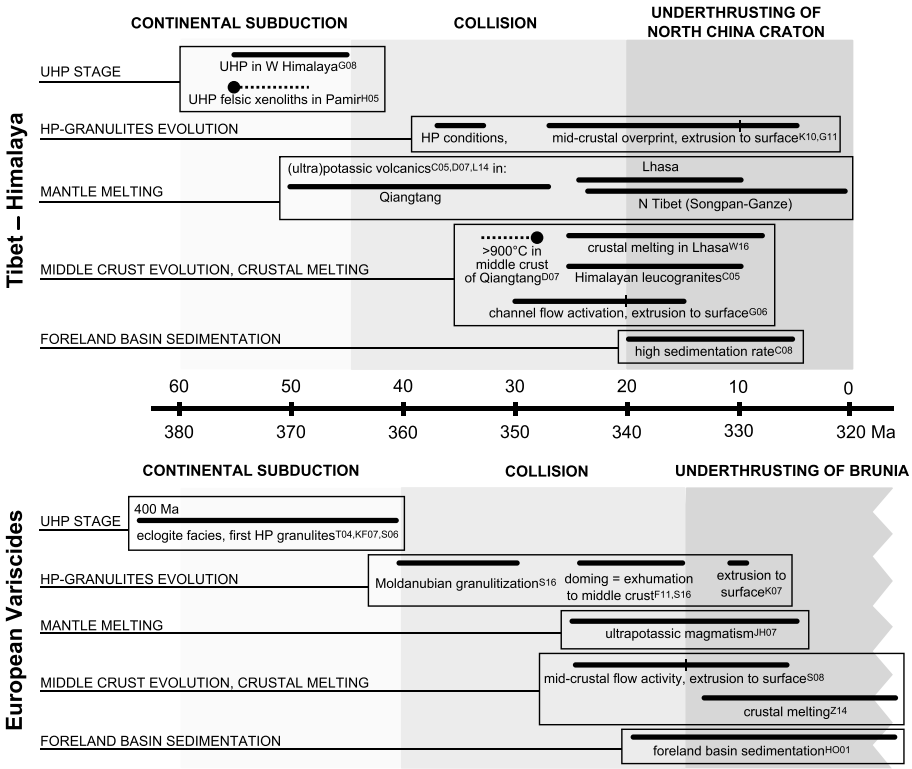

Figure 3. Comparison of timing and duration of different processes during collision in Tibet-Himalaya and European Variscides. (top) Data for Tibet-Himalaya are from *Chung et al.* [2005] (C05), *Clift et al.* [2008] (C08), *Ding et al.* [2007] (D07), *Godin et al.* [2006] (G06), *Guillot et al.* [2008] (G08), *Guilmette et al.* [2011] (G11), *Hacker et al.* [2005] (H05), *Kali et al.* [2010] (K10), *Liu et al.* [2014] (L14), and *Weller et al.* [2016] (W16). (bottom) Data for European Variscides are from *Friedl et al.* [2011] (F11), *Hartley and Otava* [2001] (HO01), *Janoušek and Holub* [2007] (JH07), *Kotková* [2007] (K07), *Kryza and Fanning* [2007] (KF07), *Schneider et al.* [2006] (S06), *Schulmann et al.* [2008] (S08), *Štípská et al.* [2016] (S16), *Timmermann et al.* [2004] (T04), and *Žák et al.* [2014] (Z14).

The timing of the granulitization and crustal melting beneath the Tibetan Plateau is not well constrained due to the lack of direct evidence. In western Tibet (Pamir), conditions of up to ~28 kbar at ~1050°C were identified for crustal xenoliths in ultrapotassic lavas intruding the southern margin of the Qiangtang terrane [*Hacker et al.*, 2005]. The age of the granulite facies metamorphism was constrained to 57–11 Ma (with the latter age corresponding to the volcanic eruption) and can be attributed to the early stages of the continental collision [*Hacker et al.*, 2005]. In Central Tibet (south Qiangtang), mafic granulites witnessed temperatures of 900–1000°C at 13–14 kbar before 28 Ma [*Ding et al.*, 2007]. In South Tibet, adakitic magmatism suggests that by 40 Ma, the crust was already thickened and granulitized [*Guo et al.*, 2012]. Direct evidence of crustal melting at about 25 Ma in South Tibet is given by local exhumation of middle crust [*Weller et al.*, 2016]. The age data for granulites and (ultra)potassic volcanism are summarized in Figures 2 and 3.

2.1.2. Tectonic Evolution

Geological conceptual models suggest that Tibet was built from Gondwana-derived continental terranes, initially separated by oceanic basins. In Mesozoic times, they were successively amalgamated, from north to south, to the southern margin of Eurasia. This scenario is confirmed by occurrence of southward younging oceanic sutures between the individual blocks and obducted Tethyan ophiolites in South Tibet [*Yin and Harrison*, 2000]. The end of amalgamation and beginning of continental collision were marked by arrival of the Indian continent at 60–55 Ma.

The Tibetan crust thickens due to northward and southward underthrusting of strong cratonic lithospheres of India and Asia, respectively, and underthrusting of individual blocks between the Asian-Indian jaws at a convergent rate of 4–7 cm/yr since 50 Ma [e.g., *van Hinsbergen et al.*, 2011]. The following detailed scenario

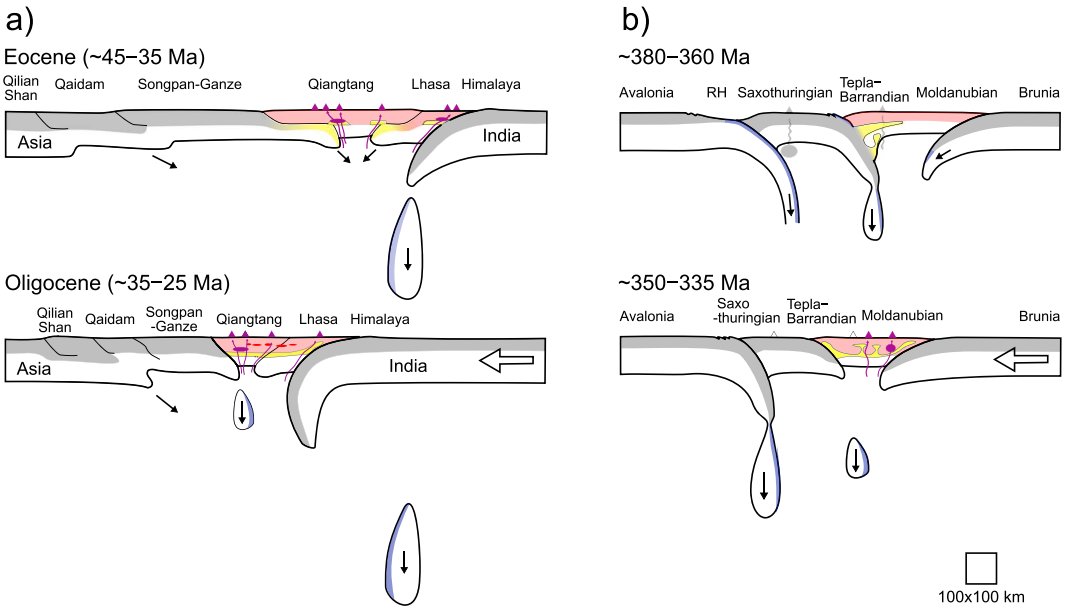

Figure 4. Comparative geodynamic scenarios for the TH system and European Variscides showing similar length and time scales of collisional processes (modified after *Guillot and Replumaz* [2013] and *Schulmann et al.* [2014]. (a) TH: Relamination of the Songpan-Ganze and Lhasa lower crust beneath the Qiangtang block and relamination of the Indian crust beneath the Lhasa block (top). The onset of extrusion of hot lower crust in the Himalaya and onset of midcrustal melting (red) in Tibet (bottom). The ascent and accumulation of (ultra)potassic magma is in violet. (b) Variscides: The relamination stage marking influx of Saxothuringian felsic crust (yellow) beneath the upper plate (Moldanubian–Teplá-Barrandian crust) (top). Gravity-driven redistribution of the relaminated material and activation of the midcrustal horizontal flow forced by indentation of Brunia (bottom). This stage is accompanied by massive emplacement of (ultra)potassic magmas in the root domain (violet). For detailed description see text in section 2.

for the growth of the Tibetan Plateau was proposed by *Guillot and Replumaz* [2013] based on available geophysical, geological, and petrological data (Figure 4a). The collision started due to northward continental subduction (soft collision) of the north Indian margin beneath the intraoceanic arc and the south Asian active margin between ~60 and ~45 Ma. It led to the formation and exhumation of UHP continental rocks. In South Central Tibet, the hard collision between ~45 and ~20 Ma was characterized by synchronous underthrusting of (1) the Indian margin beneath the Lhasa terrane, (2) the north Lhasa terrane beneath the south Qiangtang, and (3) the Songpan-Ganze terrane beneath the north Qiangtang terrane [*Kapp et al.*, 2003] (Figure 4a, top). The emplacement of the Indian continental crust beneath the Lhasa terrane was proposed already by *Argand* [1924], and proven by seismic surveys [e.g., *Nelson et al.*, 1996; *Nábělek et al.*, 2009]. Similarly, the Songpan-Ganze allochthon traveled far beneath the Qiangtang terrane in the opposite direction [e.g., *Kapp et al.*, 2003]. This process called relamination was defined by *Hacker et al.* [2011] and involves subduction of buoyant continental crust that is later detached from the subduction channel and redistributed to the base of the upper plate crust. Such a mechanism was modeled already by *Chemenda et al.* [2000] to explain crustal thickening of the Tibetan Plateau. *Guillot and Replumaz* [2013] argued that these processes resulted into granulitization of the fertile relaminated metasedimentary materials, nowadays observed as HP granulite xenoliths trapped by ultrapotassic volcanics [e.g., *Hacker et al.*, 2014].

Synchronously with the underthrusting along the base of the crust, the shortening of the system was accommodated by moderate nappe stacking in the upper crust [*Tapponnier et al.*, 1990; *Kapp et al.*, 2007]. At around 30–25 Ma, the excess of gravity potential energy of the Tibetan Plateau resulted in activation of channel flow (Figure 4a, bottom), eventually leading to extrusion of midcrustal rocks along the southern Himalayan front between 20 and 15 Ma [e.g., *Godin et al.*, 2006]. The high topography and wet climate resulted into intense erosion along the flank of the Plateau and sedimentation in the Bengal and Indus fans [e.g., *Clift et al.*, 2008]. In the present day, the deformation of the crust beneath the Tibetan Plateau is dominated by distributed ductile flow as shown by Global Positioning System data [*Zhang et al.*, 2004].

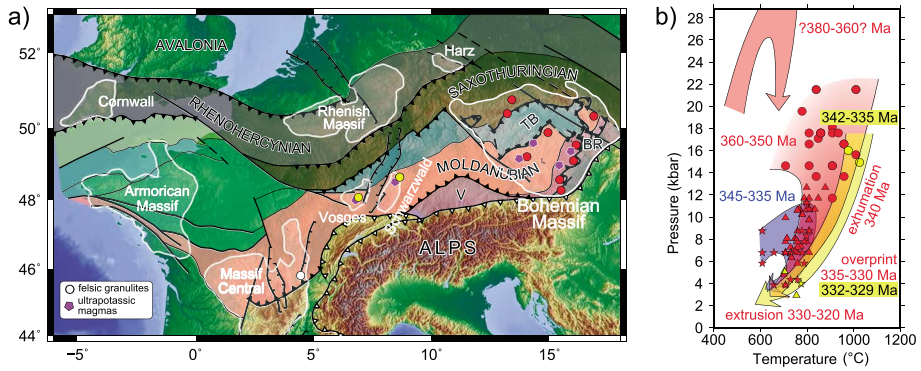

Figure 5. European Variscides: geotectonic map and *P-T*(-time) conditions. (a) Geotectonic map of the eastern-central European Variscides with positions of terranes, main sutures, and thrust zones. Distribution of (ultra)potassic plutonic rocks (purple pentagons) and high-pressure rocks in gneiss domes (circles) is also shown. White outlines show positions of Variscan outcrops. TB = Teplá-Barrandian; North-Gondwana-derived blocks: BR = Brunia, V = Vindelicia. (b) Red path shows evolution of HP granulites and high-temperature eclogites from peak conditions (red and yellow circles) (e.g., *O'Brien and Rötzler* [2003], *Schulmann et al.* [2008], and references therein, *Faryad and Žák* [2016], and references therein, for the Bohemian Massif, and *Marschall et al.* [2003], for Schwarzwald) toward their re-equilibration (triangles) with surrounding migmatites (asterisks) [*Schulmann et al.*, 2008, and references therein]. The UHP path was interpreted to record a preceding evolutionary stage [*Faryad and Žák*, 2016]. Blue path depicts the evolution of the middle crust [e.g., *Štípská et al.*, 2008; *Petri et al.*, 2014]. Colors of symbols correspond to those in Figure 5a.

2.2. European Variscides

2.2.1. Geology and Geophysics

The European Variscan orogenic belt is a fossil collisional zone with current length and width of ~3000 and ~800 km, respectively (Figure 5a). The eastern branch of the European Variscides is characterized by well exposed moderately to deeply eroded sections in the Bohemian Massif, Schwarzwald, and Vosges that show a similar orogenic architecture and geological history [*Kossmat*, 1927]. The central high-grade part of the eastern Variscides is represented by the Moldanubian domain marked by a low Bouguer gravity anomaly, low seismic reflectivity, and low seismic velocity above the Moho and was interpreted as a former orogenic root [*Guy et al.*, 2011]. In the outer southeastern part, a positive Bouguer anomaly was detected suggesting presence of high-density continental crust underneath a thin layer of light rocks of the former root [*Edel and Weber*, 1995].

A characteristic feature of the Moldanubian domain is the presence of largely melt undepleted, felsic high-pressure granulites with Ordovician-Silurian granitic protoliths [*Janoušek et al.*, 2004] and of mostly Visean metamorphic age accompanied by voluminous (ultra)potassic plutons (circles and pentagons in Figure 5a) [*Janoušek and Holub*, 2007]. The origin of these magmas was attributed to melting of metasomatized/crustally contaminated mantle and mixing of such anomalous mantle-derived melts with crustally derived magmas [e.g., *Holub*, 1997]. At the eastern front of the Bohemian Massif, the high-pressure rocks, surrounded by migmatites, are cropping out in a narrow channel-like structure [*Štípská et al.*, 2008].

The metamorphic evolution of the Variscan orogenic root resulted from superposition of distinct stages [*Schulmann et al.*, 2014]. The earliest stage (~400–370 Ma) is well recorded by eclogitic nappes emplaced over the continental lower plate (e.g. in the Mariánské Lázně Complex [*Timmermann et al.*, 2004]) and by some HP felsic granulites (e.g., in Góry Sowie, *Kryza and Fanning* [2007]; *Schneider et al.* [2006]). In the Moldanubian domain in a strict sense, early eclogite facies metamorphism and/or granulitization is suggested to occur already at around 355 Ma [e.g., *Štípská et al.*, 2016]. The metamorphic climax and main exhumation stage recoded in HP granulites and high-temperature eclogites took place at ~340 Ma [e.g., *Friedl et al.*, 2011; *Štípská et al.*, 2016]. It was characterized by UHP conditions [e.g., *Kotková et al.*, 2011], decompression to ~18 kbar where widespread re-equilibration occurred, and was followed by almost isothermal decompression to ~6 kbar (red and yellow paths in Figure 5b) [*O'Brien and Rötzler*, 2003; *Marschall et al.*, 2003]. Synchronously, midcrustal rocks underwent prograde evolution up to ~10 kbar and 700°C (blue path in Figure 5b) [e.g., *Petri et al.*, 2014]. All these rocks were then re-equilibrated together with surrounding migmatites in the middle crust at around 700°C (triangles and asterisks in Figure 5b) [e.g., *Štípská et al.*, 2008]. This late event was accompanied by intrusion of anatectic granitoids into shallow crustal levels [*Žák et al.*, 2014].

2.2.2. Tectonic Evolution

The tectonic evolution of the Caledonian-Variscan belt started with successive Silurian to Devonian amalgamation of continental Gondwana-derived terranes ultimately resulting in formation of the Pangea supercontinent [*Murphy and Nance*, 2008]. The boundaries of microblocks are characterized by presence of SE younging oceanic sutures [*Stampfli et al*., 2013]. The whole collage (Avalonia, Armorica, and Saxothuringia in the east) and north Gondwana were subsequently shortened during Carboniferous convergence between Laurussia and Gondwana forming a thickened root especially in the Moldanubian domain.

The Variscan orogeny in eastern-central Europe started with eastward subduction of the Saxothuringian oceanic and later on continental lithosphere beneath a continental plate of Gondwanan provenance (Teplá-Barrandian and Moldanubian domains) at ~380–360 Ma (Figure 4b, top). The collision began when the Saxothuringian continental lithosphere was fully underthrust beneath the upper plate at ~360–350 Ma (Figure 4b, top). This event was coeval with the onset of subduction of the Rhenohercynian oceanic lithosphere to the west [*Shail and Leveridge*, 2009] and activation of westward subduction of the Brunia continental lithosphere in the east. *Lexa et al*. [2011] suggested that the peak of crustal thickening in the root domain coincided in time with relamination of the Saxothuringian felsic crust underneath the Teplá-Barrandian-Moldanubian plate (yellow, Figure 4b). This event was followed by diachronous ascent of the relaminated lower crust in a form of crustal-scale domes at ~345–335 Ma along the whole length and width of the Moldanubian domain (Figure 4b, bottom) [*Schulmann et al*., 2014, and references therein]. Finally, symmetric underthrusting of continental blocks at ~335–325 Ma resulted in development of subhorizontal midcrustal flow connected with extrusion of the former lower crust over the indentors toward the surface. The exhumation of these rocks is also connected to the development of a giant (Silesian) turbiditic sedimentary fan covering a significant part of the underthrust Brunia domain [*Hartley and Otava*, 2001].

3. Comparison of the two Systems

The precursor of both the Tibetan and Moldanubian thickening was progressive amalgamation of Gondwanan continental fragments to the northern hemispheric land mass (Figure 1). The volume of the continental lithosphere amalgamated with the northern continental mass was comparable (~3000 km in length ~1000 km width) for the European tract of the Variscan belt and TH. The geodynamic position of Gondwanan fragments during amalgamation and collision (Figure 1) was almost identical, and large plate velocities were estimated for the collisional stages of both TH and Variscan orogenies [*van Hinsbergen et al*., 2011; *Edel et al*., 2013]. In both cases we observe a time sequence of eclogite facies metamorphism, granulite facies metamorphism, ultrapotassic magmatism, midcrustal flow, exhumation of granulites, crustal melting, extrusion of high-grade rocks to the surface, and intense foreland basin sedimentation (Figure 3). Noticeably, the Variscan high mountains were located close to the equator and were facing to the south during the Carboniferous [*Edel et al*., 2013] indicating similar climatic conditions as those required for focused erosion on the southern slopes of the Himalayas [*Hodges*, 2000]. Certainly, differences can be found in several respects, namely, it is the early ultrapotassic volcanism in the Qiangtang terrane, which was probably related to the sequential amalgamation of continental blocks in Central Tibet [*Tapponnier et al*., 2001]. In addition, in the European Variscides the relationship between the formation of the earliest ~400 Ma HP granulites (Góry Sowie) and the distinct 340 Ma peak of the granulite facies metamorphism is not satisfactorily explained.

In the TH the whole orogenic history finishes by amalgamation of the Indian block to the northern continental landmass (Figure 1), while in the Variscan Europe the amalgamation of Armorican or Hun terranes [*Stampfli et al*., 2013] to northern Laurussia was partly obliterated by final collision of Gondwana and Laurussia supercontinents together with the previously attached continental blocks at ~330–290 Ma [*Edel et al*., 2013]. This last event related to the formation of the Pangea supercontinent affected mainly the southern European (Italian, French, and Spanish) realm [*Gutiérrez-Alonso et al*., 2008; *Chopin et al*., 2014]. Therefore, the comparison made in this paper is restricted to the 380–330 Ma part of Variscan history which geodynamically matches convergence of the Asian landmass and the Indian subcontinent.

Besides the similarities in the inferred large-scale tectonic evolution we point out recent petrological observations which have never been compared before and which provide a new basis to study the relationship between tectonic processes occurring in fossil and modern hot orogens.

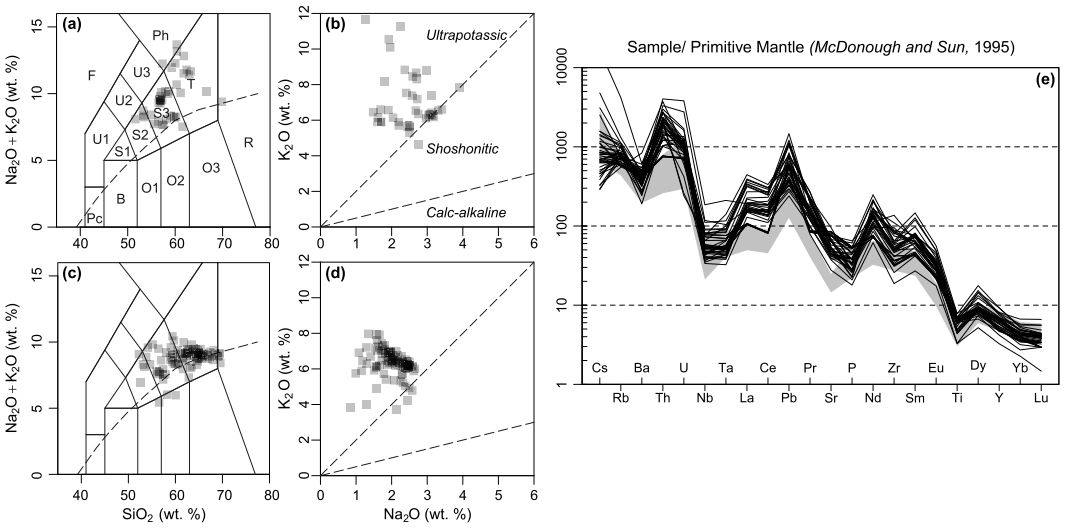

Figure 6. Comparing compositions of (ultra)potassic igneous rocks from (a and b) South Tibet (Lhasa Block) [*Ding et al*., 2003; *Zhao et al*., 2009] and the (c and d) Variscan Bohemian Massif [*Holub*, 1997; *Janoušek and Holub*, 2007, and unpublished]. Figures 6a and 6c show total alkalis-silica [*Le Bas et al*., 1986] classification diagram: F = foidite, Pc = picrobasalt, B = basalt, O1 = basaltic andesite, O2 = andesite, O3 = dacite, S1 = trachybasalt, S2 = basaltic trachyandesite, S3 = trachyandesite, T = trachyte/trachydacite, R = rhyolite, U1 = tephrite/basanite, U2 = phonotephrite, U3 = tephriphonolite, and Ph = phonolite. The dashed dividing line between alkaline and subalkaline domains is after *Irvine and Baragar* [1971]. Figures 6b and 6d show binary plot Na_2O versus K_2O (weight) to distinguish ultrapotassic rocks. (e) Primitive Mantle [*McDonough and Sun*, 1995] normalized spiderplot for (ultra)potassic volcanics from South Tibet [*Ding et al*., 2003; *Zhao et al*., 2009]. Gray background field portrays variability of Bohemian (ultra)potassic rocks taken from *Janoušek and Holub* [2007].

1. The Cenozoic Tibetan (ultra)potassic volcanites containing crustal xenoliths can represent surface equivalents of the Carboniferous (ultra)potassic plutons spatially and temporally associated with HP granulites in the Moldanubian domain [*Janoušek and Holub*, 2007]. The association of granulites and (ultra)potassic magmatites indicates the presence of felsic rocks in the deep orogenic lower crust and melting of previously contaminated lithospheric mantle beneath.
2. In the Moldanubian domain and South Tibet, these (ultra)potassic igneous rocks show mutually comparable major-element compositions (Figures 6a–6d). Characteristic are also large-ion lithophile elements/high field strength elements enrichments in the Primitive Mantle-normalized spiderplots (Figure 6e) and crust-like Sr-Nd-Pb isotopic signatures even in the most basic members. This requires an origin from strongly enriched lithospheric mantle domains, most likely contaminated by mature crustal material [*Becker et al*., 1999; *Ding et al*., 2007; *Janoušek et al*., 2010; *Janoušek and Holub*, 2007; *Zhao et al*., 2009].
3. The granulite xenoliths from the Tibetan (ultra)potassic volcanites reveal peak pressure conditions matching those retrieved from the granulites in the European Variscides including near-UHP conditions from far-western Tibet (Pamir) [*Hacker et al*., 2005] (Figure 2b, squares and Figure 5b, circles). Also, the *P-T* data from the south Tibetan-Himalayan and European-Variscan granulites, eclogites, and their host rocks reveal striking similarities for peak and re-equilibration conditions (Figures 2b and 5b, circles, triangles, and asterisks). The comparison of these data points to similar processes of burial, exhumation, and re-equilibration in both orogens.
4. In both systems, the orogenic middle crust bears evidence of widespread partial melting. In Tibet, the presence of partial melt has been deduced mainly by geophysical methods and supported by petrological data pointing to Cenozoic midcrustal melting [e.g., *Weller et al*., 2016]. In the European Variscides such a zone is observed directly and is dominated by midcrustal migmatites [*Žák et al*., 2014].
5. Of particular importance is the question of re-equilibration of HP rocks in midcrustal depth at elevated temperatures in the core of the orogens. In the Variscan orogen, such hot decompression was repeatedly demonstrated [e.g., *O'Brien and Rötzler*, 2003; *Štípská et al*., 2008]. In the TH orogen, midcrustal re-equilibration is well documented in the Himalayan granulites [e.g., *Kali et al*., 2010; *Zhang et al*., 2010], but petrological features in the Tibetan xenoliths that may be interpreted as a result of tectonic decompression before extraction by magma are rare [*Jolivet et al*., 2003]. However, midcrustal conditions

calculated [*Hacker et al*., 2000] or inferred [*Ding et al*., 2007; *Chan et al*., 2010] from xenoliths and their ages spanning from 28 to 0.5 Ma imply that even in Tibet, the rocks may have been exhumed to middle crust in early stages of the hard collision, i.e. 10 to 15 Myr before activation of channel flow in southern Tibet.

These geological observations suggest that crustal-scale dynamics and mechanisms leading to formation of individual observed rock types and specific thermal conditions are similar in both orogens. The common processes are the deep-crustal relamination of felsic lower crust [*Kapp et al*., 2003; *Hacker et al*., 2011; *Lexa et al*., 2011] and the midcrustal flow of partially molten rocks [*Beaumont et al*., 2001; *Štípská et al*., 2008]. Even if the channel flow as it was defined in Tibet cannot be unambiguously identified in the Variscan belt due to deep erosion of the crustal lid, the midcrustal flow was recurrently demonstrated together with focused sedimentation of HP granulites along the orogenic margin [*Schulmann et al*., 2008]. A geodynamic process linking the relamination and midcrustal flow was so far described and modeled only for the European Variscan belt and called the laterally forced gravity overturns [*Lexa et al*., 2011]. This process is driven by inverted density stratification and brings the relaminated felsic lower crust to midcrustal levels, where it is incorporated into the channel flow during the ongoing collision.

Based on the above described similarities of the Variscan and Tibetan orogens, we suggest that the gravity overturns could govern dynamics of the thickened continental crust also in Tibet. In order to test this possibility, we will demonstrate the efficiency of the gravity overturns by numerical experiments.

4. Numerical Models of Lower Crustal Exhumation

Numerical models of the TH system have mostly focused on orogen-scale dynamics, formation of the plateau, and underlying lithospheric processes. The lack of constraints on the internal crustal structure prevented modelers from adding more complexities into the models. However, as shown by the recent geological data, the Tibetan crust is far more heterogeneous than expected, and the heterogeneities may have a strong impact on its dynamics. Here we test whether a crustal heterogeneity resulting from relamination could explain the observed metamorphism in the TH system. As a starting point, we will summarize the main results of two numerical modeling studies [*Jamieson et al*., 2004; *Maierová et al*., 2014] where crustal dynamics in correlation with *P-T* evolution were examined in the modern TH and Variscan Bohemian Massif, respectively.

4.1. Previous Studies

The metamorphic evolution in the TH system was studied by *Jamieson et al*. [2004]. They set up a 2-D thermomechanical model of collision of two lithospheric plates, where the flow in the mantle is approximated kinematically and deformation is modeled only in the crust. In their model, a thick and hot orogenic root gradually develops. The high temperature in the root weakens the material and in synergy with surface denudation focused on topographic slopes causes the material to form a channel flowing laterally toward the topographic front. The *P-T* history of the material exhumed at the surface (peak pressures and temperatures up to ~14 kbar and 800°C, respectively) is comparable to the conditions inferred from the Himalayan migmatites. Conditions corresponding to granulitic metamorphism were attained only in the lower crust. This material was then partially uplifted by the approaching crustal indentor and entrained into the channel, but it never (until 54 Myr of model evolution) reached a level higher than ~40 km depth (>10 kbar).

Jamieson et al. [2004] took into account viscosity and heat productivity variations but neglected buoyancy forces within the crust. This is in contrast with important density variations directly observed in the Bohemian Massif: now at the surface, the orogenic lower crust contains low-density felsic rocks (~2.67 g/cm^3; granulite, orthogneiss) in tight contact with denser mafic rocks (~2.8 g/cm^3; amphibolite), while the ambient middle crust shows intermediate densities (~2.73 g/cm^3). Respecting these observations, *Maierová et al*. [2014] modeled the Paleozoic tectonic evolution of the Bohemian Massif. They adopted a similar approach as *Jamieson et al*. [2004], but it takes into account the presence of felsic (rheologically weak, low-density, heat productive) lower crust which is initially overlain by a mafic (strong, high-density) layer inducing gravitational instability. The inverted density stratification in conjunction with lateral compression induces exhumation not only in the vicinity of the crustal indentor but also deep in the root, where buckling of the rheologically strong layer and buoyancy-driven vertical exchanges of the middle and lower crust take place. The resulting peak *P-T* conditions in the root are comparable to those observed in the exhumed lower crust of the Bohemian Massif (~18 kbar and ~800°C) and the paths show a typical two-stage evolution with

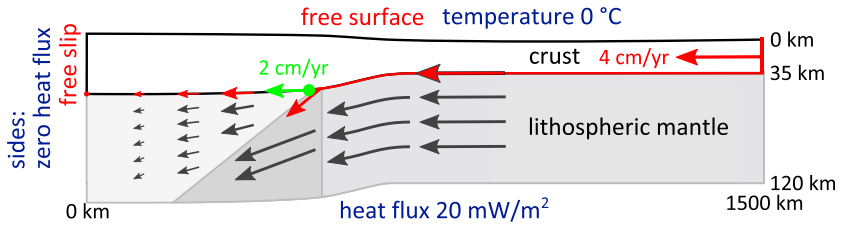

Figure 7. Model setup and boundary conditions. The model is vertically divided into crust and mantle lithosphere. In the crust, the right block moves leftward with the velocity of 4 cm/yr and plays a role of a stiff indentor, while the left block develops into a thickened orogenic root. The position of the contact between the root and the indentor at the base of the crust moves 2 cm/yr toward left (green arrow). At the base of the root, the tangential velocity decreases from 2 cm/yr at the contact with the indenter to 0 cm/yr at the left boundary. The velocity in the mantle (grey arrows) is prescribed kinematically. The crust contains several distinct materials with viscoplastic rheology. The initial distribution of materials is shown in Figures 8 and 9 for each model separately. Details of implementation of surface processes, isostatic compensation and kinematic flow in the lithospheric mantle are in the supporting information.

isothermal decompression followed by cooling at midcrustal conditions. Only a minor part of the middle crust is affected by channel flow and exhumed all the way to the surface.

The comparison of these studies implies that inherited density variations may have an important effect on tectonic and metamorphic evolution of an orogen, and they can potentially explain also the observed exhumation of HP rocks in Tibet and Himalaya. In the European Variscides, the densities and other key properties of the felsic lower crust are well described thanks to abundances of these rocks at the surface. This is not the case in the TH system, and therefore, our numerical models mainly examine the effect of the lower crustal properties on the exhumation process and corresponding *P-T* paths.

4.2. Model Setup

We model collision of two lithospheric blocks. The model setup and values of parameters (e.g., spatial scale, velocity of convergence, and erosion efficiency) approximately agree with the observed characteristics of the TH system. As argued in the previous section, they might be valid for the European Variscides as well, but in the case of the currently active orogeny they are better constrained. In many aspects, our model is inspired by models of *Beaumont et al.* [2001] and *Jamieson et al.* [2004], but we applied several modifications which influence the model behavior. The most important (but not the only) modification is the incorporation of density variations and density inversion in the crust.

We summarize here the main characteristics of the model; a detailed description of the model setup including governing equations and parameter values is given in the supporting information. We consider a plane-strain thermomechanical lithospheric-scale model. We implement it into an extended version of the software Elmer (www.csc.fi/english/pages/elmer), which uses a combination of the finite element and particle-in-cell methods. The computational grid can deform to follow the evolving surface topography and flexure of the crust-mantle boundary, which mimics isostatic compensation of the crustal load. The model domain is discretized into 500×55 quadrilateral bilinear elements with an increased resolution in the crust. A sketch of the model setup and boundary conditions is in Figure 7.

The modeled heat transport includes advection and diffusion of heat, viscous dissipation, and radiogenic heat sources. The deformation of material is solved only in the upper (crustal) part of the model, while in the lower (mantle) part we assume a kinematically prescribed velocity. The internal body forces in the crust result from prescribed constant densities of individual materials; the density changes due to temperature variations are neglected. The crust is modeled as an incompressible viscoplastic material. In the viscous regime it behaves like a fluid with a non-Newtonian temperature-dependent viscosity. If the stress reaches the yield stress given by the Drucker-Prager yield criterion, material enters the plastic regime, where the stress is equal to the yield stress. The list of the main material parameters is in Table 1.

The model domain is vertically divided into two blocks. To the left is the future "orogenic root," which corresponds to the amalgamated terranes in Tibet prior to collision with India. To the right is a strong continental block ("indentor") representing the Indian microcontinent. The reference model (model A) contains three crustal layers in each block. The upper two layers ("upper and middle crust," grey and brown material in

Table 1. Material Parameters in Models A and B

	Viscosity[a] (Flow Law)	Melting?	Density[b] (g cm^{-3})	Heat Sources[c] (10^{-6} Wm^{-3})	Initial Thickness[d] (km)
Left Block ("Crustal Root")					
Upper crust	"wet quartz"	yes	2.7	2	10
Middle crust	"wet quartz × 3"	yes	2.75	1.5	15
Mafic lower crust	"basalt × 0.1"	no	2.8	0.75	10
Right Block ("Indentor")					
Upper crust	"wet quartz"	yes	2.7	2	10
Middle crust	"wet quartz × 5"	yes	2.75	1.5	15
Mafic lower crust	"basalt"	no	2.8	0.75	10
Felsic Lower Crust ("Relaminant")					
	"wet quartz"	no	2.7	2	5

[a]The viscosity is determined using the parameters by *Gleason and Tullis* [1995] (wet quartz) and *Mackwell et al.* [1998] (wet Maryland diabase—basalt). The scaling of the viscosity (e.g., "wet quartz × 3") is performed by multiplication of the pre-exponential factor by the given constant.
[b]The density of the mafic lower crust is modified by "eclogitization" as described in section 4.2.
[c]The heat sources linearly decrease between 750 and 900°C and they are zero above the latter temperature. This switch off simulates extraction of radiogenic elements by melt, and it is irreversible.
[d]In the regions where the felsic lower crust is present the thickness of the middle crust and mafic lower crust is reduced to 12 km and 8 km, respectively.

Figures 8 and 9) have a felsic composition modeled by a weak rheology. The bottom layer ("lower crust," green material in Figures 8 and 9) is modeled using parameters for a mafic material (Table 1). In the felsic material we also take into account weakening due to partial melting. It is modeled as a linear decrease of viscosity by 1 order of magnitude between 700 and 750°C.

Density is constant in each layer, except for the mafic lower crust at high pressures. This material undergoes eclogitization, which we parametrize as a linear increase of density from the initial value to 3.2 g cm^{-3} between pressures of 14 and 18 kbar [cf. *Hetényi et al.*, 2007]. The density of 3.2 g cm^{-3} at pressures higher than 18 kbar is the same as the mantle density. Such a pressure-dependent density increase has an important effect on the vertical position of the crust-mantle boundary, the boundary between the mafic and felsic material in the root, and on the surface topography. Similarly to the density, also the intensity of radiogenic heating is material dependent (Table 1).

In the reference model (model A), the material is stratified so that the density increases or is constant with depth at the beginning of the simulation. In other models (models of type B), we test the effect of felsic low-density material placed into the lower crust. This material (yellow in Figures 8 and 9) represents the relaminant emplaced beneath the mafic lower crust during initial stages of collision. The composition of the relaminant is expected to be felsic in analogy to the European Variscides, where such lower crustal rocks—felsic granulites—are present in large volumes. We assume that properties of the relaminant (density, viscosity, and heat sources) are the same as those of the upper crust. The only difference is that the lower crustal material cannot be further weakened by melting. In reality, the rheology of these rocks can be very complex, as witnessed by the Moldanubian felsic granulites. Their microstructures show evidence of grain size sensitive creep and very low effective viscosity, despite the fact that only a small percentage of melt was present [*Janoušek et al.*, 2004; *Franěk et al.*, 2011a].

The collision of the "root" and the "indentor" is induced by conditions prescribed at the boundaries of the crustal domain (Figure 7). The left boundary of the model (at $x = 0$ km) is an impermeable free-slip boundary. In a first approximation, it plays the role of a strong backstop, such as a strong continental block. The velocity of the indentor is 4 cm/yr (toward left). It is prescribed as a normal velocity at the right boundary and tangential velocity at the base of the crust of the indentor. The value of 4 cm/yr is comparable to the current convergence rate between India and Asia [e.g., *Tapponnier et al.*, 2001; *van Hinsbergen et al.*, 2011]. It is therefore somewhat lower than the long term average of this rate [*van Hinsbergen et al.*, 2011]. Using this low value in the model is justified by the fact that a part of the convergence was accommodated by lateral flow which cannot be captured by the presented two-dimensional models.

The initial position of the contact between the two blocks is at $x = 1200$ km, and it moves 2 cm/yr toward left. At the base of the left block, the tangential velocity linearly changes between 2 cm/yr at the contact of the blocks toward zero at $x = 0$ km. Such boundary condition represents homogeneous thickening of the

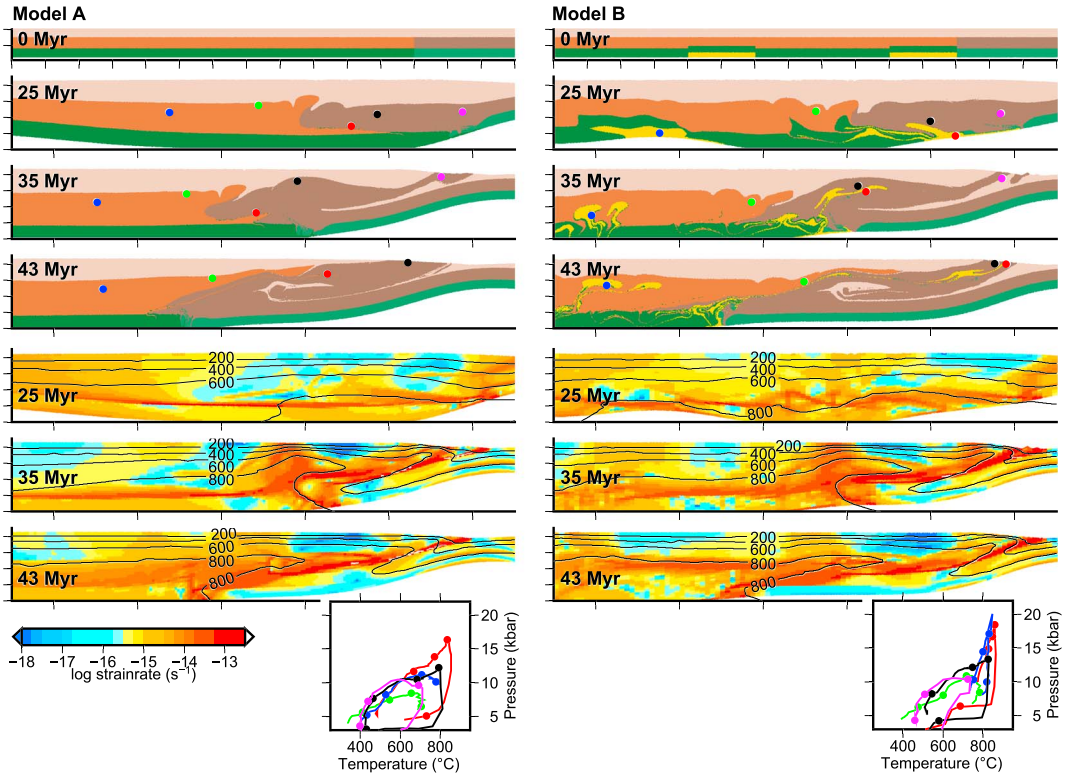

Figure 8. Material distribution (top four rows of panels), isotherms and strain rate (bottom three rows of panels) in three representative time steps in (left) model A and (right) model B. The time from the beginning of the model evolution is noted in top left part of each panel. Tics on the *x* and *y* axes are every 100 and 20 km, respectively. The top row for each model shows initial material distribution in the crust (note the different *x* scale). Temperature contours are every 200°C. The inset panels show *P-T* paths of selected particles. Points show *P-T* conditions at 10 Myr steps. Positions of the particles are shown in the material plot using the same colors as for the *P-T* paths.

lithospheric mantle, which is a deformational style consistent with the expected weak mantle below Central Tibet (Qiangtang terrane) [e.g., *Jiménez-Munt et al.*, 2008]. The crust-mantle boundary is impermeable except a short region right of the contact of the blocks. There the material flows out of the crust and induces subduction of the lower crust of the indentor. This approach prevents unrealistic accumulation of the lower crustal material near the contact [*Jamieson et al.*, 2004]. The total velocity of convergence is thus equally divided into the motion of the contact and subduction of the lower crust.

During the time evolution, the shape of the top model boundary changes, being modeled as a free surface. The resulting surface topography is modified by slope-and-time-dependent erosion and topography-dependent sedimentation. The erosion is proportional to the topographic slope, and therefore, it is focused to the flanks of the orogen. In addition, we assume that erosion efficiency is reduced to the left of a high topography (surface elevated to more than 4 km above the zero level). This corresponds to the wet climate and efficient erosion to the south of the Tibetan Plateau, and lack of erosion at the Plateau [e.g., *Hodges*, 2000]. The rate of erosion (at a certain slope) increases with time, mimicking the increasingly wet climate during the Miocene [e.g., *Clift et al.*, 2008]. The vertical position of the crust is further corrected for the effect of isostasy by an analytically calculated deformation of the lithosphere.

Boundary conditions for heat transport are: temperature of 0 °C at the top, zero heat flux on sides and influx of 20 mW/m^2 at the bottom of the domain. The initial temperature field is calculated as a stationary temperature for boundary conditions and material properties valid for the reference model (i.e., the initial temperature field is the same in all models). During the time evolution we use a kinematically prescribed velocity of material in the lithospheric mantle to calculate heat advection. The prescribed velocity field approximates leftward motion and subduction of the right block, motion of the contact between the blocks and homogeneous thickening in the root.

4.3. Results

First we describe evolution of the model without density inversion in the lower crust. In this model (model A, Figure 8, left column) we initially observe progressive crustal thickening near the contact of the colliding blocks associated with accumulation of heat produced by radiogenic heat sources (25 and 35 Myr). In the upper crust, a high-temperature gradient develops, while the lower crust shows nearly isothermal conditions. Eventually, the growing potential energy of the overthickened root, temperature-induced weakening of the material, and erosion focused at the topographic front lead to extrusion of the middle crust toward the surface (35 and 43 Myr). The extrusion is associated with channel flow in the midcrustal levels, doming of the weak middle crust and extension of the upper crust. The fast advection of material and heat results into inversion of isotherms and high-temperature gradient below the orogenic flank.

At the end of the simulation, high *P-T* conditions are recorded by the material deep in the root and above the ramp of the indentor (~17 kbar, red particle). In the root the material records only negligible decompression (blue particle), and the peak metamorphic conditions depend mainly on the initial depth of the particle. Starting from ~33 Myr, the highest temperature attained by the material at the surface exceeds 700°C (magenta particle), and ~10 Myr later it reaches ~800°C (black particle). Peak pressures recorded by this material are ~12 kbar.

Model B (Figure 8, right column) has the same properties as model A, but a felsic "relaminated" material is emplaced at the base of the crust of the left block. It is located in two 200 km long regions. The first region is near the contact of the blocks, which is the position where the India-derived relaminant beneath the Lhasa block could reside. The second one is further in the root and may represent the relaminant beneath Qiangtang.

Evolution of this model shares the first order characteristics with model A, namely, the lower crustal thickening and the development of an elevated geotherm. However, the internal architecture of the root and *P-T* conditions recorded by material particles differ significantly. The shortening and thickening of the root is accompanied by folding of the mafic lower crust and redistribution of the felsic crust (25 Myr). This deformation evolves into gravity-driven doming of the felsic lower crust (FLC) and its emplacement into the middle crust (35 Myr). The heterogeneous middle crust including deformed FLC bodies is then exhumed along a ramp formed by the strong material of the right crustal block (43 Myr).

In the root, the low viscosity of the hot felsic material results into high strain rates and it is thus responsible for mechanical decoupling of the rigid upper crust (superstructure) from the deeper orogenic levels (infrastructure) [*Culshaw et al.*, 2006]. This zone of decoupling, hereafter referred to as the infrastructure-superstructure transition zone, is defined as a horizon of intense deformation. In contrast to the model A, in model B it is associated with mixing of lower crustal and middle crustal rocks and heat advected from depth. The lateral flow in this zone and the exhumation of high-grade rocks is enhanced by deep underthrusting of the rigid block to the right.

The *P-T* paths recorded by the FLC exhumed to the surface (red particle) show three stages: heating and pressure increase, nearly isothermal decompression, and cooling during the final extrusion. Peak conditions of ~18 kbar ~850°C are achieved at ~30 Myr. The isothermal decompression ends at ~7–5 kbar, where significant cooling begins and the slope of the *P-T* path changes. In the root, the stage of extrusion is missing and the FLC achieves higher peak pressures (~20 kbar, blue particle), because the exhumation is not triggered by the arrival of the indentor. The evolution of the middle crust far from the FLC is practically the same as in model A (green, magenta, and black particles). This model also documents that the *P-T* paths in the extruded FLC and in the nearby middle crust can show very contrasting peak conditions (~18 kbar at ~850°C and ~13 kbar at ~800°C, red and black particles, respectively).

We further test the sensitivity of model B to the character of the lower crust. We vary density and viscosity of the FLC (models B-Fd20 and B-Fv3) and increase the viscosity of the mafic lower crust (model B-Mv1). Besides that we test the effect of stronger melt weakening of the middle crust (model B-Melt100). The specific model parameters are listed in Table 2, and the resulting material and *P-T* evolutions are presented in Figure 9.

In model B, the density of the FLC is by 50 kg m^{-3} lower than that of the middle crust. With a smaller density contrast of 20 kg m^{-3}, the incorporation of the FLC into the middle crust is more difficult (model B-Fd20 in Figure 9). Below the topographic plateau, the reduction of the density contrast causes an increase of the depth of emplacement and final pressure (~10 kbar instead of ~8 kbar, compare blue particles in models B-Fd20 and B). Near the indentor, the FLC is still near the base of the crust at 35 Myr. Later it is exhumed thanks to lateral forcing to ~5 kbar, but it has not reached the surface at the end of the simulation (43 Myr).

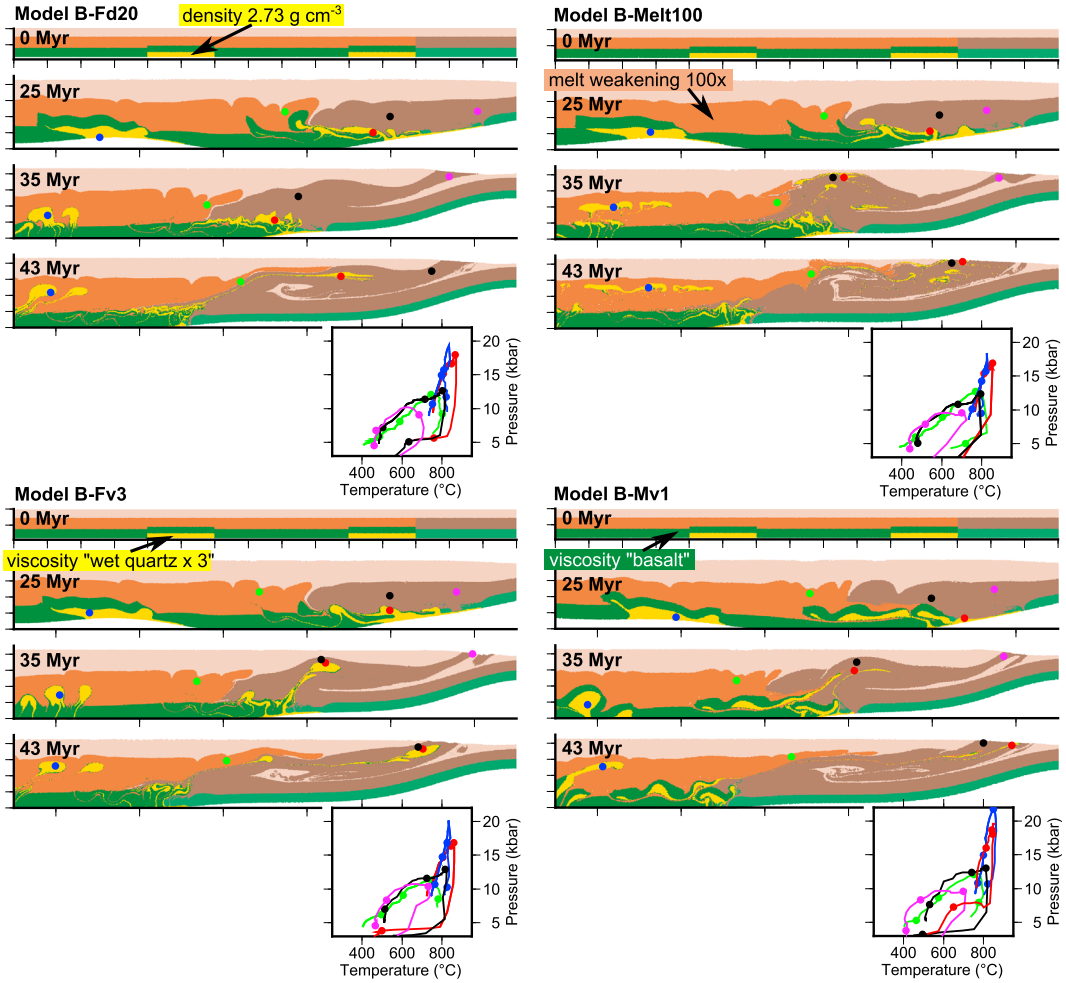

Figure 9. Material distribution in three representative time steps in models B-Fd20, B-Fv3, B-Mv1, and B-Melt100. See text in section 4.3 and Tables 1 and 2 for the description of the models. Tics on the *x* and *y* axes are every 100 and 20 km, respectively. The top row for each model shows initial material distribution in the crust (note the different *x* scale). The time from the beginning of the model evolution is noted in the top left part of each panel. The inset panels show *P-T* paths of selected particles. Points show *P-T* conditions at 10 Myr steps. Positions of the particles are shown in the material plot using the same colors as for the *P-T* paths.

We assume that the relaminated lower crust has a felsic composition, but even a felsic material can have a strong rheological behavior, for example, if it is a granulitic residuum. We test such a case by increasing the viscosity of the FLC three times (model B-Fv3 in Figure 9). In the root the uprising FLC forms relatively stronger and less deformed bodies within the weak middle crust. Even during extrusion toward the surface the FLC bodies keep their rounded shape. An opposite situation occurs if the FLC and the middle crust can mix easily. Such a deformation style is present, for example, if we assume that partial melting causes a more pronounced decrease of viscosity (100-fold decrease, model B-Melt100 in Figure 9). In that case the FLC bodies are quickly disintegrated in the middle crust. Despite the contrasting architecture of the middle crust, the overall evolution and *P-T* paths in models B-Fv3 and B-Melt100 are similar.

Table 2. Specific Parameters of Models in Figure 9[a]

Model	Specific Parameter
B-Fd20	felsic lower crust density 2.73 g cm^{-3}
B-Fv3	felsic lower crust viscosity "wet quartz × 3"
B-Mv1	mafic lower crust in the left block—viscosity "basalt × 1"
B-Melt100	melt weakening 100×

[a]Other parameters are the same as in model B.

We further test the effect of the viscosity of the mafic lower crust. If this viscosity is high (model B-Mv1 in Figure 9), this strong layer hinders the exhumation of the FLC. In contrast to the previous models, significant

portions of the FLC, mainly near the contact of the colliding blocks, remain in the lower crust until the end of the simulation. Nevertheless, thin FLC slivers are incorporated into the midcrustal flow and exhumed to the surface. This material resided at the bottom of the root for a prolonged period of time, and due to continuous crustal thickening, it records very high peak pressures (~20 kbar, red particle). Pressures attained by the FLC bodies underneath the topographic plateau are even higher (~22 kbar, blue particle).

It is noteworthy that in the models of type B, the FLC is accompanied by mafic material detached from the lower crust. It typically forms thin rims around the FLC bodies (e.g., model B-Fv3). The proportion of this material is small, but the FLC penetration through the lower crust appears to be a possible mechanism for exhumation of mafic lower crustal material to the surface.

5. Discussion

5.1. Model Summary

The main conclusion which can be drawn from our experiments is that the model without density inversion (model A, Figure 8, left column) can hardly satisfy the metamorphic evolution of the orogenic lower crust in the European Variscides and in the TH. The lower crust exhumation in this model occurs only along the rigid indentor, and the rocks in the internal part of the orogen reveal continuous thickening over a long time interval. Peak pressures of ~13 kbar are compatible with the conditions characteristic of the Himalayan migmatites but not of the granulites. In contrast, the models with density inversion (e.g., model B, Figure 8, right column) can capture both the exhumation of HP rocks across the whole width of the orogen and the characteristic features of the *P-T* paths including peak pressures of more than 18 kbar.

Even a minor density inversion between the "relaminated" FLC and the middle crust can induce the overturn of the FLC and the overlying layers (model B-Fd20 in Figure 9). Of course, the main density contrast which triggers the exhumation process is between the felsic and mafic lower crust. This contrast is essential and results from the different composition of the standard lower crust and the relaminant. For a mafic relaminant, the gravity-driven exhumation is not a viable mechanism. The overturn of the felsic lower and middle crust is feasible only if the latter is sufficiently weak. In a large hot orogen, this is ensured by weakening due to partial melting. The viscosity of the felsic material affects also the degree of mixing of the FLC with the middle crust layers (compare models B-Fv3 and B-Melt100 in Figure 9). As a result, the FLC exhumed along the ramp of the indentor can have different appearance: it can form rounded bodies or thin slivers, or it may have irregular unsharp boundaries.

The model evolution takes ~43 Myr which is a comparable time span to the ~50–10 Ma evolution in the TH system. At ~30 Myr, the midcrustal rocks with maximum temperatures above 700°C and pressures ~10 kbar appear at the surface. At about the same time the FLC bodies are incorporated into the middle crust, and their exhumation to the surface occurs ~10 Myr later. This sequence is in agreement with the ages of metamorphism of migmatites and granulites in the Himalaya. The timing of channel flow and exhumation of high-grade material is similar in all studied models with density inversion. This is due to the same velocity of convergence and erosion rate imposed in these models.

Our models illustrate the process of gravity-driven exhumation and its sensitivity to the density and viscosity structure of the lower crust. In a realistic model of a large hot orogen, also other processes should be present, such as the preceding amalgamation of lithospheric blocks. The amalgamation and relamination during early continental collision are crucial for the development of the inverted density stratification and the related instability. This orogenic stage can be very complex, and its incorporation into the model would require tuning of many parameters that are only vaguely constrained. In contrast, we decided to keep the initial model setup as simple as possible. We therefore omit the division of the root into several blocks resulting from amalgamation. Besides that, we neglect the perturbation of the initial temperature field due to the previous dynamic evolution and namely due to the emplacement of the relaminant. Actually, this temperature perturbation is difficult to determine, because the relaminant can experience thermally contrasting paths in the mantle—along the subducting plate or through the mantle wedge. We can only speculate that this stage is recorded in the early (U)HP metamorphism of some of the granulites.

In the model, the felsic middle and lower crust is exhumed to the surface via a combination of channel flow, doming and extension of the upper crust described by *Beaumont et al*. [2001]. The occurrence of these deformation styles is rather sensitive to the model parameters, namely, the erosion rate and viscosity of the middle and upper crust. The channel flow is not a focus of our study, and we do not test the influence of these parameters systematically. Besides that, the comparison of models A and B suggests that the influence of the lower crustal overturns on the dynamics of the subsequent midcrustal flow is not very strong. This probably results from the fact that the proportion of the FLC in the orogenic root and in the extruding channel is only minor in our models.

The effect of convergence velocity and radiogenic heating in a similar model setup was studied by *Maierová et al*. [2014]. They showed that the amount of the radiogenic heat mainly affects the peak temperatures, but the radiogenic heat also weakens the crust leading to earlier and more intense deformation. The velocity of convergence provides additional forcing of the buoyancy-driven exchanges and speeds up the lower crustal evolution; a faster convergence results into lower peak temperatures and higher peak pressures. However, it also importantly influences the later exhumation of the middle (and lower) crust toward the surface. The character of exhumation crucially depends on the interplay between the convergence and erosion rates [cf. *Beaumont et al*., 2001]. We adopted the value of the maximum erosion efficiency for a certain slope from the models by *Jamieson et al*. [2004]. With this value we obtain rates of maximum ~1 cm/yr of material removal at the plateau flank in the presented models.

Another process that is essential for the development of the channel flow is the melting of the orogenic middle crust [e.g., *Beaumont et al*., 2001]. In the model the melting is extremely simplified: we prescribe a linear viscosity decrease proportional to a temperature-dependent melt content, and we neglect melt extraction, migration and solidification entirely. Melt extraction may, however, lead to formation of dry granulitic residuum and increase the viscosity of the material. Neglecting this effect is in our view justified by observations. The migmatized middle crust in the Moldanubian zone and in the Himalaya suggests that melt extraction (if present) did not cause formation of high-viscosity granulitic residuum at this crustal level [*Štípská et al*., 2008]. The situation is more complex in the case of the lower crust. The melting of the Moldanubian granulites was probably only minor and yet they remained extremely weak in the lower crust, and their strength increased when they reached midcrustal levels [*Franěk et al*., 2011b]. This behavior might be, however, specific to the Moldanubian granulites.

Melting and solidification further induce perturbation of the temperature field due to latent heat consumption and release. Crustal melting does not change the total heat budget of the crust, but the melt can bring heat upward closer to the surface and thus enhance cooling. In contrast, the rising mantle-derived magmas provide an important heat addition into the crust. Geological data show that melt migration and interaction between the mantle and crust played an important role during the formation of the European Variscides and the TH system. Incorporation of these processes into a numerical model requires a different strategy than the one adopted here and remains to be a subject for a future study.

5.2. Deep-Crustal Architecture of the Modeled Orogen

The presented observations and models suggest that not only the Variscan but also the Tibetan crust can be highly heterogeneous and may result from an unstable density stratification inherited from a relamination process. In Figure 10, we summarize an internal architecture of the modeled orogen and describe it using a terminology valid for the geology of both studied orogenic systems. We propose that the main features observed in the model may be present both in the European Variscides and in the TH system.

The uppermost 20 km of the crust with temperatures below 600°C is the superstructure formed by steeply folded upper crustal rocks and sediments. The layer in between 20 and 40 km depth corresponds to the infrastructure-superstructure transition zone. Its upper part is dominated by partially molten metasediments of the upper plate and horizontal sheets of anatectic granitoids emplaced just beneath the superstructure. The lower part comprises felsic granulites together with lenses of mafic rocks, retrograded eclogites, and intrusions of ultrapotassic magmas. The vertical advection of heat during the formation of this zone contributes to elevation of the geotherm and increase of the surface heat flow. It would be imaged as a low-resistivity zone, while the horizontal granitic intrusions can correspond to the bright spots. The low-velocity zone would extend deeper, containing the lobes of upper plate migmatized metasediments and relics of

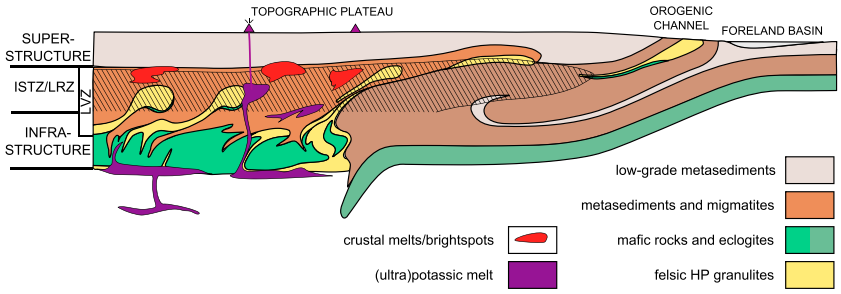

Figure 10. Deep crustal structure of a conceptual large hot orogen derived from the numerical model and the Bohemian Massif geology. The infrastructure is formed by a deep layer of eclogites (green) and lobes of granulitized metasediments (brown) and high-pressure (HP) granulites. The infrastructure-superstructure transition zone (ISTZ) consists of a layer of recrystallized HP granulites (yellow), retrograded eclogites (green), amphibolites (green), and migmatized sediments (brown) of the upper plate. In the orogenic root the ISTZ coincides with the low-resistivity zone (LRZ, hatched), while the low-velocity zone (LVZ) extends deeper. The boundary between the superstructure (gray) and the ISTZ is marked by horizontal sheets of anatectic granitoids and leucogranites (red). Mantle-derived (ultra)potassic magma (purple) batches are syntectonically emplaced in the ISTZ and connected with volcanoes at the surface.

felsic granulites. The heterogeneity of the infrastructure-superstructure transition zone with alternating dry granulites and partially molten metasediments is in line with the discontinuous character of the low-velocity zone observed in Tibet [*Hetényi et al*., 2011].

The deepest part of the crust consists of a layer of eclogitized mafic metavolcanics [*Hetényi et al*., 2007; *Schulmann et al*., 2014]. This complex in between 40 and 80 km depth represents the orogenic infrastructure. Important feature captured in Figure 10 is the formation of the ultrapotassic magma by melting of metasomatized mantle and its emplacement into the middle crust. During its ascent, the magma is contaminated by the crustal component and it samples HP rocks from the infrastructure and retrograded granulites and migmatites from the middle crust which are transported with volcanites in form of xenoliths to the surface.

6. Conclusions

We reviewed new observations and concepts which improve the comparison between modern and ancient orogenic belts. We show that the Variscan and Tibetan-Himalayan orogens share fundamental similarities, some of which have escaped unnoticed so far:

1. The geodynamic scenarios including amalgamation of microblocks (Figure 1) and subsequent collisional processes are almost identical in terms of duration and length scales (Figures 3 and 4).
2. The *P-T* evolution of the lower crustal rocks reveals matching peak conditions up to 18 kbar and 800°C (without considering UHP subduction stage) as well as re-equilibration at midcrustal pressures of ~6–10 kbar suggesting that both burial and exhumation processes in both regions were of similar nature (Figures 2b and 5b).
3. The granulite facies metamorphism is connected to (ultra)potassic magmatism, composition of which testifies for contamination of anomalous metasomatized mantle by mature crustal material (Figure 6).
4. Petrological, structural, and geophysical evidence of midcrustal horizontal flow of partially molten rocks was reported for both orogenic systems.

Besides that, the same tectonic processes were invoked for the crustal evolution of the two orogens: relamination of allochthonous low-density felsic lower crust beneath "parautochthonous" terranes and later development of midcrustal flow. It is proposed here that the two processes are linked by gravity overturns bringing the relaminated material to midcrustal depths. Such overturns were previously considered to explain the observations in the European Variscides, but their consideration also in the case of Tibet and Himalaya can provide a new perspective on this modern orogen. Numerical experiments show that even a weak density inversion in the modeled lower crust can trigger the gravity redistribution within the root domain and successfully reproduce the petrological observations. In our models, the partially molten middle crust is highly heterogeneous and has a polyphase tectonic history due to interplay between buoyancy-driven redistribution and continental underthrusting.

The present work provides fresh insight into deep architecture of the Tibetan Plateau using both the knowledge of the deeply eroded Bohemian Massif and the crustal processes inferred from the numerical model. We argue that for further improvement of knowledge on modern orogens, the limited information based on the plate tectonic paradigm and lithospheric-scale geophysical observations may be insufficient, and more constraints such as structural, petrological, and geochronological data available in fossil orogens are needed. By incorporating these data into numerical models, we may better understand the multistage evolution of modern orogens.

Acknowledgments
This work is a contribution to the project "DSP-Tibet" funded by the Agence Nationale de la Recherche (ANR-13-BS06-012-01) and to the LK11202 program of the Ministry of Education of the Czech Republic awarded to K.S. We also acknowledge financial support through the Czech National Grant Agency (P210-13-16315S). We would like to thank to Jeroen van Hunen, Lars Kaislaniemi, and an anonymous reviewer. Their comments helped to enhance the quality of the manuscript significantly.

References

Alsdorf, D., L. Brown, K. D. Nelson, Y. Makovsky, S. Klemperer, and W. Zhao (1998), Crustal deformation of the Lhasa terrane, Tibet Plateau from Project INDEPTH deep seismic reflection profiles, *Tectonics*, *17*, 501–519, doi:10.1029/98TC01315.

Argand, E. (1924), La tectonique de l'Asie, *C. R. Congr. Géol. Int.*, *1*(5), 171–372.

Artemieva, I. M. (2006), Global 1°X1° thermal model TC1 for the continental lithosphere: Implications for lithosphere secular evolution, *Tectonophysics*, *416*, 245–277, doi:10.1016/j.tecto.2005.11.022.

Beaumont, C., R. A. Jamieson, M. H. Nguyen, and B. Lee (2001), Himalayan tectonics explained by extrusion of a low-viscosity crustal channel coupled to focused surface denudation, *Nature*, *414*, 738–742, doi:10.1038/414738a.

Beaumont, C., R. A. Jamieson, J. P. Butler, and C. J. Warren (2009), Crustal structure: A key constraint on the mechanism of ultra-high-pressure rock exhumation, *Earth Planet. Sci. Lett.*, *287*, 116–129, doi:10.1016/j.epsl.2009.08.001.

Becker, H., T. Wenzel, and F. Volker (1999), Geochemistry of glimmerite veins in peridotites from Lower Austria—Implications for the origin of K-rich magmas in collision zones, *J. Petrol.*, *40*, 315–338, doi:10.1093/petroj/40.2.315.

Brown, L. D., W. Zhao, K. D. Nelson, M. Hauck, D. Alsdorf, A. Ross, M. Cogan, M. Clark, X. Liu, and J. Che (1996), Bright spots, structure, and magmatism in Southern Tibet from INDEPTH seismic reflection profiling, *Science*, *274*, 1688–1690, doi:10.1126/science.274.5293.1688.

Chan, G. H. N., D. J. Waters, M. P. Searle, J. C. Aitchison, M. Horstwood, Q. G. Crowley, C. H. Lo, and J. S. L. Chan (2010), Probing the basement of southern Tibet: Evidence from crustal xenoliths entrained in a Miocene ultrapotassic dyke, *J. Geol. Soc. London*, *166*(1), 45–52, doi:10.1144/0016-76492007-145.

Chemenda, A. I., J. P. Burg, and M. Mattauer (2000), Evolutionary model of the Himalaya–Tibet system: Geopoem based on new modelling, geological and geophysical data, *Earth Planet. Sci. Lett.*, *174*, 397–409, doi:10.1016/S0012-821X(99)00277-0.

Chopin, F., M. Corsini, K. Schulmann, M. El Houicha, J. F. Ghienne, and J. B. Edel (2014), Tectonic evolution of the Rehamna metamorphic dome (Morocco) in the context of the Alleghanian-Variscan orogeny, *Tectonics*, *33*, 1154–1177, doi:10.1002/2014TC003539.

Chung, S. L., M. F. Chu, Y. Zhang, Y. Xie, C. H. Lo, T. Y. Lee, C. Y. Lan, X. Li, Q. Zhang, and Y. Wang (2005), Tibetan tectonic evolution inferred from spatial and temporal variations in post-collisional magmatism, *Earth Sci. Rev.*, *68*, 173–196, doi:10.1016/j.earscirev.2004.05.001.

Clift, P. D., K. V. Hodges, D. Heslop, R. Hannigan, H. Van Long, and G. Calves (2008), Correlation of Himalayan exhumation rates and Asian monsoon intensity, *Nat. Geosci.*, *1*, 875–880.

Collins, W. J. (2003), Slab pull, mantle convection, and Pangaean assembly and dispersal, *Earth Planet. Sci. Lett.*, *205*, 225–237, doi:10.1016/S0012-821X(02)01043-9.

Culshaw, N. G., C. Beaumont, and R. A. Jamieson (2006), The orogenic superstructure–infrastructure concept: Revisited, quantified, and revived, *Geology*, *34*, 733–736, doi:10.1130/G22793.1.

Dewey, J. F., and K. C. A. Burke (1973), Tibetan, Variscan, and Precambrian basement reactivation: Products of continental collision, *J. Geol.*, *81*, 683–692, doi:10.1086/627920.

Ding, L., P. Kapp, D. L. Zhong, and W. M. Deng (2003), Cenozoic volcanism in Tibet: Evidence for a transition from oceanic to continental subduction, *J. Petrol.*, *44*, 1833–1865, doi:10.1093/petrology/egg061.

Ding, L., P. Kapp, Y. Yue, and Q. Lai (2007), Postcollisional calc-alkaline lavas and xenoliths from the southern Qiangtang terrane, central Tibet, *Earth Planet. Sci. Lett.*, *254*, 28–38, doi:10.1016/j.epsl.2006.11.019.

Dörr, W., and G. Zulauf (2010), Elevator tectonics and orogenic collapse of a Tibetan-style plateau in the European Variscides: The role of the Bohemian shear zone, *Int. J. Earth Sci.*, *99*, 299–325, doi:10.1007/s00531-008-0389-x.

Dymkova, D., T. Gerya, and J.-P. Burg (2016), 2D thermomechanical modelling of continent–arc–continent collision, *Gondwana Res.*, *32*, 138–150, doi:10.1016/j.gr.2015.02.012.

Edel, J. B., and K. Weber (1995), Cadomian terranes, wrench faulting and thrusting in the central Europe Variscides: Geophysical and geological evidence, *Geol. Rundsch.*, *84*, 412–432, doi:10.1007/BF00260450.

Edel, J. B., K. Schulmann, E. Skrzypek, and A. Cocherie (2013), Tectonic evolution of the European Variscan belt constrained by palaeomagnetic, structural and anisotropy of magnetic susceptibility data from the Northern Vosges magmatic arc (eastern France), *J. Geol. Soc. London*, *170*, 785–804, doi:10.1144/jgs2011-138.

England, P., and D. McKenzie (1982), A thin viscous sheet model for continental deformation, *Geophys. J. Int.*, *70*, 295–321, doi:10.1111/j.1365-246X.1982.tb04969.x.

Faryad, S. W., and J. Žák (2016), High-pressure granulites of the Podolsko complex, Bohemian Massif: An example of crustal rocks that were subducted to mantle depths and survived a pervasive mid-crustal high-temperature overprint, *Lithos*, *246*, 246–260.

Franěk, J., K. Schulmann, O. Lexa, S. Ulrich, P. Štípská, J. Haloda, and P. Týcová (2011a), Origin of felsic granulite microstructure by heterogeneous decomposition of alkali feldspar and extreme weakening of orogenic lower crust during the Variscan orogeny, *J. Metamorph. Geol.*, *29*, 103–130, doi:10.1111/j.1525-1314.2010.00911.x.

Franěk, J., K. Schulmann, O. Lexa, Č. Tomek, and J. B. Edel (2011b), Model of syn-convergent extrusion of orogenic lower crust in the core of the Variscan belt: Implications for exhumation of high-pressure rocks in large hot orogens, *J. Metamorph. Geol.*, *29*, 53–78, doi:10.1111/j.1525-1314.2010.00903.x.

Friedl, G., R. Cooke, F. Finger, N. McNaughton, and I. R. Fletcher (2011), Timing of Variscan HP–HT metamorphism in the Moldanubian Zone of the Bohemian Massif: U–Pb SHRIMP dating on multiply zoned zircons from a granulite from the Dunkelsteiner Wald Massif, Lower Austria, *Mineral. Petrol.*, *102*, 63–75, doi:10.1007/s00710-011-0162-x.

Gerya, T., and B. Stöckhert (2006), Two-dimensional numerical modeling of tectonic and metamorphic histories at active continental margins, *Int. J. Earth Sci.*, *95*, 250–274, doi:10.1007/s00531-005-0035-9.

Gerya, T. V., L. L. Perchuk, D. D. Van Reenen, and C. A. Smit (2000), Two-dimensional numerical modeling of pressure ± temperature-time paths for the exhumation of some granulite facies terrains in the Precambrian, *J. Geodyn.*, *30*, 17–35, doi:10.1016/S0264-3707(99)00025-3.

Gleason, G. C., and J. Tullis (1995), A flow law for dislocation creep of quartz aggregates determined with the molten salt cell, *Tectonophysics*, *247*(1-4), 1–23, doi:10.1016/0040-1951(95)00011-B.

Godin, L., D. Grujic, R. D. Law, and M. P. Searle (2006), Channel flow, ductile extrusion and exhumation in continental collision zones: An introduction, *Geol. Soc. London, Spec. Publ.*, *268*, 1–23, doi:10.1144/GSL.SP.2006.268.01.01.

Gray, R., and R. N. Pysklywec (2012), Geodynamic models of mature continental collision: Evolution of an orogen from lithospheric subduction to continental retreat/delamination, *J. Geophys. Res.*, *117*, B3408, doi:10.1029/2011JB008692.

Groppo, C., B. Lombardo, F. Rolfo, and P. Pertusati (2007), Clockwise exhumation path of granulitized eclogites from the Ama Drime range (Eastern Himalayas), *J. Metamorph. Geol.*, *25*, 51–75, doi:10.1111/j.1525-1314.2006.00678.x.

Guillot, S., and A. Replumaz (2013), Importance of continental subductions for the growth of the Tibetan Plateau, *Bull. Soc. Geol. Fr.*, *184*, 199–223, doi:10.2113/gssgfbull.184.3.199.

Guillot, S., G. Mahéo, J. de Sigoyer, K. H. Hattori, and A. Pêcher (2008), Tethyan and Indian subduction viewed from the Himalayan high- to ultrahigh-pressure metamorphic rocks in the Himalaya, *Tectonophysics*, *451*, 225–241, doi:10.1016/j.tecto.2007.11.059.

Guilmette, C., A. Indares, and R. Hébert (2011), High-pressure anatectic paragneisses from the Namche Barwa, Eastern Himalayan Syntaxis: Textural evidence for partial melting, phase equilibria modeling and tectonic implications, *Lithos*, *124*, 66–81, doi:10.1016/j.lithos.2010.09.003.

Guo, L., H. F. Zhang, B. W. Harris, R. Parrish, W. C. Xu, and Z. L. Shi (2012), Paleogene crustal anatexis and metamorphism in Lhasa terrane, eastern Himalayan syntaxis: Evidence from U–Pb zircon ages and Hf isotopic compositions of the Nyinchi complex, *Gondwana Res.*, *21*, 100–111, doi:10.1016/j.gr.2011.03.002.

Gutiérrez-Alonso, G., J. Fernández-Suárez, A. B. Weil, J. B. Murphy, R. D. Nance, F. Corfú, and S. T. Johnston (2008), Self-subduction of the Pangaean global plate, *Nat. Geosci.*, *1*, 549–553.

Guy, A., J.-B. Edel, K. Schulmann, Č. Tomek, and O. Lexa (2011), A geophysical model of the Variscan orogenic root (Bohemian Massif): Implications for modern collisional orogens, *Lithos*, *124*, 144–157, doi:10.1016/j.lithos.2010.08.008.

Hacker, B. R., E. Gnos, L. Ratschbacher, M. Grove, M. McWilliams, S. V. Sobolev, J. Wan, and W. Zhenhan (2000), Hot and dry deep crustal xenoliths from Tibet, *Science*, *287*, 2463–2466, doi:10.1126/science.287.5462.2463.

Hacker, B. R., P. Luffi, V. Lutkov, V. Minaev, L. Ratschbacher, T. Plank, M. Ducea, A. Patiño-Douce, M. McWilliams, and J. Metcalf (2005), Near-ultrahigh pressure processing of continental crust: Miocene crustal xenoliths from the Pamir, *J. Petrol.*, *46*, 1661–1687, doi:10.1093/petrology/egi030.

Hacker, B. R., P. B. Kelemen, and M. D. Behn (2011), Differentiation of the continental crust by relamination, *Earth Planet. Sci. Lett.*, *307*, 501–516, doi:10.1016/j.epsl.2011.05.024.

Hacker, B. R., M. H. Ritzwoller, and J. Xie (2014), Partially melted, mica-bearing crust in Central Tibet, *Tectonics*, *33*, 1408–1424, doi:10.1002/2014TC003545.

Hartley, A. J., and J. Otava (2001), Sediment provenance and dispersal in a deep marine foreland basin: The Lower Carboniferous Culm Basin, Czech Republic, *J. Geol. Soc. London*, *158*, 137–150, doi:10.1144/jgs.158.1.137.

Hetényi, G., R. Cattin, F. Brunet, L. Bollinger, J. Vergne, J. L. Nábělek, and M. Diament (2007), Density distribution of the India plate beneath the Tibetan plateau: Geophysical and petrological constraints on the kinetics of lower-crustal eclogitization, *Earth Planet. Sci. Lett.*, *264*, 226–244, doi:10.1016/j.epsl.2007.09.036.

Hetényi, G., J. Vergne, L. Bollinger, and R. Cattin (2011), Discontinuous low-velocity zones in southern Tibet question the viability of the channel flow model, *Geol. Soc. London, Spec. Publ.*, *353*, 99–108, doi:10.1144/SP353.6.

Hodges, K. V. (2000), Tectonics of the Himalaya and Southern Tibet from two perspectives, *Bull. Geol. Soc. Am.*, *112*, 324–350, doi:10.1130/0016-7606(2000)112<324:TOTHAS>2.0.CO;2.

Holub, F. V. (1997), Ultrapotassic plutonic rocks of the durbachite series in the Bohemian Massif: Petrology, geochemistry and petrogenetic interpretation, *J. Geol. Sci. Econ. Geol. Mineral.*, *31*, 5–26.

Irvine, T. N., and W. R. A. Baragar (1971), A guide to the chemical classification of the common volcanic rocks, *Can. J. Earth. Sci.*, *8*, 523–548, doi:10.1139/e71-055.

Jamieson, R. A., C. Beaumont, S. Medvedev, and M. H. Nguyen (2004), Crustal channel flows: 2. Numerical models with implications for metamorphism in the Himalayan–Tibetan orogen, *J. Geophys. Res.*, *109*, 1–24, doi:10.1029/2003JB002811.

Janoušek, V., and F. V. Holub (2007), The causal link between HP–HT metamorphism and ultrapotassic magmatism in collisional orogens: Case study from the Moldanubian Zone of the Bohemian Massif, *Proc. Geol. Assoc.*, *118*, 75–86, doi:10.1016/S0016-7878(07)80049-6.

Janoušek, V., F. Finger, M. P. Roberts, J. Frýda, C. Pin, and D. Dolejš (2004), Deciphering the petrogenesis of deeply buried granites: Whole-rock geochemical constraints on the origin of largely undepleted felsic granulites from the Moldanubian Zone of the Bohemian Massif, *Trans. R. Soc. Edinburgh: Earth Sci.*, *95*, 141–159, doi:10.1017/S0263593304000148.

Janoušek, V., F. V. Holub, T. Magna, and V. Erban (2010), Isotopic constraints on the petrogenesis of the Variscan ultrapotassic magmas from the Moldanubian Zone of the Bohemian Massif, *Mineral. - Spec. Pap.*, *37*, 32–36.

Jiménez-Munt, I., M. Fernàndez, J. Vergés, and J. P. Platt (2008), Lithosphere structure underneath the Tibetan Plateau inferred from elevation, gravity and geoid anomalies, *Earth Planet. Sci. Lett.*, *267*, 276–289, doi:10.1016/j.epsl.2007.11.045.

Jolivet, M., M. Brunel, D. Seward, Z. Xu, J. Yang, J. Malavieille, F. Roger, A. Leyreloup, N. Arnaud, and C. Wu (2003), Neogene extension and volcanism in the Kunlun Fault Zone, northern Tibet: New constraints on the age of the Kunlun Fault, *Tectonics*, *22*(10), 1052, doi:10.1029/2002TC001428.

Kali, E., P. H. Leloup, N. Arnaud, G. Maheo, D. Liu, E. Boutonnet, J. Van der Woerd, X. Liu, J. Liu-Zeng, and H. Li (2010), Exhumation history of the deepest central Himalayan rocks, Ama Drime range: Key pressure-temperature-deformation-time constraints on orogenic models, *Tectonics*, *29*, TC2014, doi:10.1029/2009TC002551.

Kapp, P., A. Yin, C. E. Manning, T. M. Harrison, M. H. Taylor, and L. Ding (2003), Tectonic evolution of the early Mesozoic blueschist-bearing Qiangtang metamorphic belt, central Tibet, *Tectonics*, *22*(4), 1043, doi:10.1029/2002TC001383.

Kapp, P., P. G. DeCelles, G. E. Gehrels, M. Heizier, and L. Ding (2007), Geological records of the Lhasa-Qiangtang and Indo-Asian collisions in the Nima area of central Tibet, *Geol. Soc. Am. Bull.*, *119*, 917–932, doi:10.1130/B26033.1.

Kind, R., J. Ni, W. Zhao, J. Wu, X. Yuan, L. Zhao, E. Sandvol, C. Reese, J. Nábělek, and T. Hearn (1996), Evidence from earthquake data for a partially molten crustal layer in Southern Tibet, *Science*, *274*, 1692–1694, doi:10.1126/science.274.5293.1692.

Kossmat, F. (1927), Gliederung des variszischen Gebirgbaues [In German], *Abh. Sächs. Geol. Landesamt*, *1*, 1–39.

Kotková, J. (2007), High-pressure granulites of the Bohemian Massif: Recent advances and open questions, *J. Geosci.*, *52*, 45–71, doi:10.3190/jgeosci.006.

Kotková, J., P. J. O'Brien, and M. A. Ziemann (2011), Diamond and coesite discovered in Saxony-type granulite: Solution to the Variscan garnet peridotite enigma, *Geology*, *39*, 667–670, doi:10.1130/G31971.1.

Kryza, R., and C. M. Fanning (2007), Devonian deep-crustal metamorphism and exhumation in the Variscan Orogen: Evidence from SHRIMP zircon ages from the HT-HP granulites and migmatites of the Góry Sowie (Polish Sudetes), *Geodin. Acta*, *20*(3), 159–175.

Le Bas, M. J., R. W. Le Maitre, A. Streckeisen, and B. Zanettin (1986), A chemical classification of volcanic rocks based on the total alkali silica diagram, *J. Petrol.*, *27*, 745–750, doi:10.1093/petrology/27.3.745.

Lexa, O., K. Schulmann, V. Janoušek, P. Štípská, A. Guy, and M. Racek (2011), Heat sources and trigger mechanisms of exhumation of HP granulites in Variscan orogenic root, *J. Metamorph. Geol.*, *29*, 79–102, doi:10.1111/j.1525-1314.2010.00906.x.

Liu, D., et al. (2014), Postcollisional potassic and ultrapotassic rocks in southern Tibet: Mantle and crustal origins in response to India–Asia collision and convergence, *Geochim. Cosmochim. Acta*, *143*, 207–231, doi:10.1016/j.gca.2014.03.031.

Mackwell, S. J., M. E. Zimmerman, and D. L. Kohlstedt (1998), High-temperature deformation of dry diabase with application to tectonics on Venus, *J. Geophys. Res.*, *103*, 975–984, doi:10.1029/97JB02671.

Maierová, P., O. Lexa, K. Schulmann, and P. Štípská (2014), Contrasting tectono-metamorphic evolution of orogenic lower crust in the Bohemian Massif: A numerical model, *Gondwana Res.*, *25*, 509–521, doi:10.1016/j.gr.2012.08.020.

Marschall, H. R., A. Kalt, and M. Hanel (2003), *P–T* evolution of a Variscan lower-crustal segment: A study of granulites from the Schwarzwald, Germany, *J. Petrol.*, *44*, 227–253, doi:10.1093/petrology/44.2.227.

Matte, P., H. Maluski, P. Rajlich, and W. Franke (1990), Terrane boundaries in the Bohemian Massif: Result of large-scale Variscan shearing, *Tectonophysics*, *177*, 151–170, doi:10.1016/0040-1951(90)90279-H.

McDonough, W. F., and S. S. Sun (1995), The composition of the Earth, *Chem. Geol.*, *120*, 223–253, doi:10.1016/0009-2541(94)00140-4.

Murphy, J. B., and R. D. Nance (2008), The Pangea conundrum, *Geology*, *36*, 703–706, doi:10.1130/G24966A.1.

Nábělek, J., G. Hetényi, J. Vergne, S. Sapkota, B. Kafle, M. Jiang, H. Su, J. Chen, B.-S. Huang, and the Hi-Climb Team (2009), Underplating in the Himalaya–Tibet collision zone revealed by the Hi-CLIMB experiment, *Science*, *325*, 1371–1374, doi:10.1126/science.1167719.

Nelson, K. D., et al. (1996), Partially molten middle crust beneath Southern Tibet: Synthesis of project INDEPTH results, *Science*, *274*, 1684–1688, doi:10.1126/science.274.5293.1684.

O'Brien, P. J., and J. Rötzler (2003), High-pressure granulites: Formation, recovery of peak conditions and implications for tectonics, *J. Metamorph. Geol.*, *21*, 3–20, doi:10.1046/j.1525-1314.2003.00420.x.

O'Brien, P. J., N. Zotov, R. Law, M. A. Khan, and M. Q. Jan (2001), Coesite in Himalayan eclogite and implications for models of India–Asia collision, *Geology*, *29*, 435–438, doi:10.1130/0091-7613(2001)029<0435:CIHEAI>2.0.CO;2.

Petri, B., P. Štípská, E. Skrzypek, K. Schulmann, M. Corsini, and J. Franěk (2014), Thermal and mechanical behaviour of the orogenic middle crust during the syn- to late-orogenic evolution of the Variscan root zone, Bohemian Massif, *J. Metamorph. Geol.*, *32*, 599–626, doi:10.1111/jmg.12081.

Pognante, U., P. Benna, and P. Le Fort (1993), High-pressure metamorphism in the High Himalayan Crystallines of the Stak valley, northeastern Nanga-Parbat-Haramosh syntaxis, Pakistan Himalaya, in Himalayan Tectonics, *Geol. Soc. Spec. Publ.*, *74*, 161–172.

Schilling, F. R., and G. M. Partzsch (2001), Quantifying partial melt fraction in the crust beneath the Central Andes and the Tibetan Plateau, *Phys. Chem. Earth, Part A Solid Earth Geod.*, *26*, 239–246, doi:10.1016/S1464-1895(01)00051-5.

Schneider, D. A., S. J. Zahniser, J. M. Glascock, S. M. Gordon, and M. Manecki (2006), Thermochronology of the west Sudetes (Bohemian Massif): Rapid and repeated eduction in the eastern Variscides, Poland and Czech Republic, *Am. J. Sci.*, *306*, 846–873.

Schulmann, K., O. Lexa, P. Štípská, M. Racek, L. Tajčmanová, J. Konopásek, J. B. Edel, A. Peschler, and J. Lehmann (2008), Vertical extrusion and horizontal channel flow of orogenic lower crust: Key exhumation mechanisms in large hot orogens?, *J. Metamorph. Geol.*, *26*, 273–297, doi:10.1111/j.1525-1314.2007.00755.x.

Schulmann, K., O. Lexa, V. Janoušek, J. M. Lardeaux, and J. B. Edel (2014), Anatomy of a diffuse cryptic suture zone: An example from the Bohemian Massif, European Variscides, *Geology*, *42*, 275–278, doi:10.1130/G35290.1.

Shail, R. K., and B. E. Leveridge (2009), The Rhenohercynian passive margin of SW England: Development, inversion and extensional reactivation, *C. R. Geosci.*, *341*, 140–155, doi:10.1016/j.crte.2008.11.002.

Stampfli, G. M., C. Hochard, C. Vérard, C. Wilhem, and J. von Raumer (2013), The formation of Pangea, *Tectonophysics*, *593*, 1–19, doi:10.1016/j.tecto.2013.02.037.

Štípská, P., K. Schulmann, and R. Powell (2008), Contrasting metamorphic histories of lenses of high-pressure rocks and host migmatites with a flat orogenic fabric (Bohemian Massif, Czech Republic): A result of tectonic mixing within horizontal crustal flow?, *J. Metamorph. Geol.*, *26*, 623–646, doi:10.1111/j.1525-1314.2008.00781.x.

Štípská, P., R. Powell, B. R. Hacker, R. Holder, and A. R. C. Kylander–Clark (2016), Uncoupled U/Pb and REE response in zircon during the transformation of eclogite to mafic and intermediate granulite (Blanský les, Bohemian Massif), *J. Metamorph. Geol.*, doi:10.1111/jmg.12193.

Tapponnier, P., B. Meyer, J. P. Avouac, G. Peltzer, and Y. Gaudemer (1990), Active thrusting and folding in the Qilian Shan, and decoupling between upper crust and mantle in northeastern Tibet, *Earth Planet. Sci. Lett.*, *97*, 382–403, doi:10.1016/0012-821X(90)90053-Z.

Tapponnier, P., X. Zhiqin, F. Roger, B. Meyer, N. Arnaud, G. Wittlinger, and Y. Jingsui (2001), Oblique stepwise rise and growth of the Tibet Plateau, *Science*, *294*, 1671–1677, doi:10.1126/science.105978.

Timmermann, H., V. Štědrá, A. Gerdes, S. R. Noble, R. R. Parrish, and W. Dörr (2004), The problem of dating high-pressure metamorphism: A U-Pb isotope and geochemical study on eclogites and related rocks of the Mariánské Lázně Complex, Czech Republic, *J. Petrol.*, *45*, 1311–1338, doi:10.1093/petrology/egh020.

Toussaint, G., E. Burov, and J. P. Avouac (2004), Tectonic evolution of a continental collision zone: A thermomechanical numerical model, *Tectonics*, *23*, 1–24, doi:10.1029/2003TC001604.

Turner, S. P., N. Arnaud, J. Liu, N. W. Rogers, C. J. Hawkesworth, N. Harris, S. P. Kelley, P. Van Calsteren, and W. Deng (1996), Post-collision, shoshonitic volcanism on the Tibetan Plateau: Implications for convective thinning of the lithosphere and the source of ocean island basalts, *J. Petrol.*, *37*, 45–71, doi:10.1093/petrology/37.1.45.

van Hinsbergen, D. J. J., B. Steinberger, P. V. Doubrovine, and R. Gassmüller (2011), Acceleration and deceleration of India-Asia convergence since the Cretaceous: Roles of mantle plumes and continental collision, *J. Geophys. Res.*, *116*, B06101, doi:10.1029/2010JB008051.

Wei, W., et al. (2001), Detection of widespread fluids in the Tibetan crust by magnetotelluric studies, *Science*, *292*, 716–719, doi:10.1126/science.1010580.

Weller, O. M., M. R. St-Onge, N. Rayner, M. P. Searle, and D. J. Waters (2016), Miocene magmatism in the Western Nyainqentanglha Mountains of southern Tibet: An exhumed bright spot?, *Lithos*, *245*, 147–160.

Willner, A. P., E. Sebazungu, T. V. Gerya, W. V. Maresch, and A. Krohe (2002), Numerical modelling of PT-paths related to rapid exhumation of high-pressure rocks from the crustal root in the Variscan Erzgebirge Dome (Saxony/Germany), *J. Geodyn.*, *33*, 281–314, doi:10.1016/S0264-3707(01)00071-0.

Yin, A., and T. M. Harrison (2000), Geologic evolution of the Himalayan–Tibetan orogen, *Annu. Rev. Earth Planet. Sci.*, *28*, 211–280, doi:10.1146/annurev.earth.28.1.211.

Žák, J., K. Verner, V. Janoušek, F. V. Holub, V. Kachlík, F. Finger, J. Hajná, F. Tomek, L. Vondrovic, and J. Trubač (2014), A plate-kinematic model for the assembly of the Bohemian Massif constrained by structural relationships around granitoid plutons, in the variscan orogeny: Extent, timescale and the formation of the European crust, *Geol. Soc. Spec. Publ.*, *405*, 169–196, doi:10.1144/SP405.9.

Zhang, P. Z., et al. (2004), Continuous deformation of the Tibetan Plateau from global positioning system data, *Geology*, *32*, 809–812, doi:10.1130/G20554.1.

Zhang, Z. M., G. C. Zhao, M. Santosh, J. L. Wang, X. Dong, and J. G. Liou (2010), Two stages of granulite facies metamorphism in the eastern Himalayan syntaxis, south Tibet: Petrology, zircon geochronology and implications for the subduction of Neo-Tethys and the Indian continent beneath Asia, *J. Metamorph. Geol.*, *28*, 719–733, doi:10.1111/j.1525-1314.2010.00885.x.

Zhao, Z., et al. (2009), Geochemical and Sr–Nd–Pb–O isotopic compositions of the post-collisional ultrapotassic magmatism in SW Tibet: Petrogenesis and implications for India intra-continental subduction beneath southern Tibet, *Lithos*, *113*, 190–212, doi:10.1016/j.lithos.2009.02.004.